Spring 2017

Application of Raman Spectroscopy to Study of Biological Systems

Neva Agarwala

APPLICATION OF RAMAN SPECTROSCOPY TO STUDY OF BIOLOGICAL SYSTEMS

A Master's Thesis

Presented to

The Graduate College of

Missouri State University

In Partial Fulfillment

Of the Requirements for the Degree

Master of Science, Materials Science

By

Neva Agarwala

May 2017

APPLICATION OF RAMAN SPECTROSCOPY TO STUDY OF BIOLOGICAL SYSTEMS

Physics, Astronomy & Materials Science

Missouri State University, May 2017

Master of Science

Neva Agarwala

ABSTRACT

Raman spectroscopy is an important tool of molecular characterization based on inelastic scattering of monochromatic light by molecules. Since Raman spectra reflect unique vibrational properties of materials, the method offers a potential of selective molecular identification. Furthermore, surface-enhanced Raman spectroscopy (SERS) also is capable of a high sensitivity, since inelastic scattering of light from the molecules is strongly enhanced when Raman-active molecules are located close to roughened noble metal surfaces. In this thesis, Raman characterization protocols of liquid biological samples are optimized. Raman spectra of two different cell cultures, yeast cells and HeLa cells, were collected and interpreted. The potentiality of SERS enhancement was tested for the cell cultures on substrates containing a plasmonic-active layer. To facilitate interpretation of Raman spectra, water-soluble carbon based materials such as graphene oxide and fullerenol also are characterized, and these results were compared with predictions of the density-functional theory. These studies have demonstrated a proof-of-principle Raman characterization of cell cultures, suggested their spectral band assignments, elucidated differences and similarities in Raman bands between the cell cultures studied, and achieved a pronounced SERS enhancement for HeLa cell analysis.

KEYWORDS: HeLa cells, yeast cells, Raman spectroscopy, SERS, molecular vibrations, DFT calculations, oxidized graphene, functionalized graphene.

This abstract is approved as to form and content

_____

Dr. Maria Stepanova
Chairperson, Advisory Committee
Missouri State University

APPLICATION OF RAMAN SPECTROSCOPY TO STUDY OF BIOLOGICAL SYSTEMS

By

Neva Agarwala

A Master's Thesis
Submitted to the Graduate College
Of Missouri State University
In Partial Fulfillment of the Requirements
For the Degree of Master of Science, Materials Science

May 2017

Approved:

_____
Dr. Maria Stepanova

_____
Dr. Kyoungtae Kim

_____
Dr. Ridwan Sakidja

_____
Dr. Julie Masterson, Dean, Graduate College

ACKNOWLEDGEMENTS

I would like to express my gratitude to my supervisor Dr. Maria Stepanova for her patience, enthusiasm, useful remarks and engagement through my entire learning process of this master's thesis. The door to Prof. Stepanova's office was always open for me whenever I had a question about my research or faced any problems. She consistently allowed this paper to be my own work, but navigated me to the right direction whenever she thought I needed it. I could not have imagined having a better advisor and mentor for my master's study.

Besides my advisor, I would also like to acknowledge other members of my thesis committee for their encouragement and insightful comments: Dr. Kim Kyoungtae for providing me yeast cells and Dr. Ridwan Sakidja for teaching me how to perform the DFT calculations.

My sincere thanks also goes to Dr. Robert Mayanovic, for helping me perform the Raman measurements and allow me to use his lab, Dr. Paul Durham and his research group, for providing me the cell culture training and sharing every single detail of cell culture with me, Dr. Kathy Fitcher, for allowing me to use her lab equipment.

Furthermore, I would like to thank the members of lab groups who I have not already mentioned: David Miley, Lauren Cornelison, John Short and Brennon Foster. They provided a friendly and cooperative atmosphere at the lab, trained me in cell culture and gave useful feedback and insightful comments on my work. I would be remiss if I did not thank Dr. Sergey Mamedov and Xueyin Yuan, provided much needed assistance with Raman instruments and measurements. In turn, Rishi Patel provided Au coating of glass slides I required.Also, Johnna Pedersen provided immediate support for any JVIC lab issues I encountered.

I am grateful for the funding sources that allowed me to pursue my graduate school studies at the Physics, Astronomy and Materials science department. I also would like to acknowledge the Department of Biology for their collaborations.

Last but not the least, I would like to thank my family: my parents Ram Abatar Agarwala and Santi Debi Agarwala, for giving me life and supporting me spiritually throughout. I would like to acknowledge my friends and family members who have supported me during my time here. Suzanne Buffington Lennard and her family, Mr. and Mrs. Burton, Renna Vincent and family, Mr. and Mrs. Hosack, Vickie Batchelder, Nicole Bowman, Claire Geneser, Sarah Nagle and Elizabeth Salley who made my time here at Springfield a lot more fun. I am lucky to have had the chance to meet all of them here, and I thank them for their friendship, love, and unyielding support. I owe a debt of gratitude to all the members of the International fellowship of which I was a member for two years.

I dedicate this thesis to my mother, Santi Debi Agarwala,
who is my main inspiration, my mentor and my idol throughout my life.
She has always supported my dreams and aspirations, and if I do say so myself,
I think she did a fine job of raising me. I would like to thank her for all she is,
and all she has done for me.

TABLE OF CONTENTS

1. Introduction 1

2. Literature Review 3
   - 2.1 Probing of Biological Materials at the Nanoscale 3
   - 2.2 The Raman Effect 5
   - 2.3 Surface Enhanced Raman Spectroscopy (SERS) 7
   - 2.4 Plasmonic Materials 9
   - 2.5 Application of Raman Spectroscopy and SERS 10
   - 2.6 Project Goals and Objectives 15

3. Methods 16
   - 3.1 Instruments 16
   - 3.2 Simulation and Visualization Software 20
   - 3.3 Cell Cultures 21

4. Experimental Design and Results 24
   - 4.1 Raman Spectroscopy of Liquid Samples 24
   - 4.2 Analysis of Vibrations in Carbon Materials 32
   - 4.3 Analysis of Cell Cultures 47

5. Discussion 60
   - 5.1 Results Achieved from This Research 60
   - 5.2 Problems Encountered During Experiments 67

6. Conclusions and Future Work 68
   - 6.1 Conclusions 68
   - 6.2 Proposed Future Works and Considerations 69

References 71

LIST OF TABLES

Table 4.1 Laser power calculations for the various magnifications 26

Table 4.2 Bond lengths for initial 9 structures before relaxation 38

Table 4.3 Bond lengths for 9 structures after optimizing of the structures.....38

Table 4.4 Comparison of experimental and predicted Raman bands 46

Table 4.5 IR and Raman band assignments in live cells.....53

Table 5.1 Raman bands positions and assignments in yeast and HeLa cells.....65

Table 5.2 Comparison of Raman band intensities in yeast and HeLa cells.....66

LIST OF FIGURES

Fig. 2.1 Energy level diagram of Raman and Rayleigh scattering 6

Fig. 2.2 A scheme of localized surface plasmon resonance 8

Fig. 2.3 Scheme of surface-enhanced Raman spectroscopy 9

Fig. 2.4 Approximate wavelength ranges where Ag, Au, and Cu nanostructures show LSPR absorption of light 10

Fig. 2.5 (a) - Silver film (200nm) over 880 nm Si nanospheres (AgFONs) on a 1-inch glass coverslip; (b) - SEM image of the system; (c) - Schematic of the acquisition apparatus..11

Fig. 2.6 Spectroelectrochemistry of a tetrathiafulvalene -derivative. Top left: molecular structure; bottom left: cyclic voltammogram in acetonitrile on a gold film over nanopsheres; right: surface-enhanced Raman spectra at different potential.....12

Fig. 2.7 Representative single-molecule SERS spectra of rhodamine 6G on silver obtained using a 532-nm excitation. (a) - Ensemble-averaged SERS obtained on an Ag island film and (b) single molecule SERS spectrum obtained on a colloidal Ag aggregate.....13

Fig. 3.1 The Motic AE31 inverted biological microscope.....16

Fig. 3.2 Fluorescent microscopic image of HeLa cells.....17

Fig. 3.3 LabRAM HR micro-Raman instrument 18

Fig. 3.4 Fume hood 20

Fig. 4.1 Scheme of experimental setup for collecting Raman spectra of liquid samples ..27

Fig. 4.2 Sample area of the LabRAM HR800 instrument 28

Fig. 4.3 Raman spectrum of pure water on Si substrate (50-4500 cm^{-1}) 30

Fig. 4.4 Raman spectra of YPD media (a biological sample) on different substrates (800-1900 cm^{-1}) 31

Fig. 4.5 Baseline extracted Raman spectra of YPD media from Fig. 4.4 31

Fig. 4.6 Normalized and baseline extracted Raman spectra of YPD media from Figs. 4.4 and 4.5.....32

Fig. 4.7 Periodic structure of graphene 34

Fig. 4.8 An oxidized graphene structure with defects obtained by replacing C atoms with O atoms. Note that the brown and red lines indicate symmetry of the initial structure, and not actual covalent bonds between the atoms 34

Fig. 4.9 Functionalized graphene with C/H ratios of (a) 8:1, (b) 8:2, and (c) 8:6 before (left) and after (right) relaxation of the structures 35

Fig. 4.10 Functionalized graphene with C/O ratios of (a) 8:1 and (b) 8:2 before (left) and after (right) relaxation of the structures 36

Fig. 4.11 Functionalized graphene with C/OH ratio of 8:1 before (left) and after (right) relaxation of the structure 37

Fig. 4.12 Predicted Raman bands of Graphene (C_8) (300-1650 cm^{-1}).....41

Fig. 4.13 Predicted Raman bands of oxidized graphene with defects (C_7O) (200-1600 cm^{-1}).....41

Fig. 4.14 Predicted Raman bands of (a) - CH_4 model (500-5000 cm^{-1}), and (b-d) - C/H models: 8:1 (300-2700 cm^{-1}), 8:2 (300-2800 cm^{-1}), and 8:6 (300-3000 cm^{-1}) 41

Fig. 4.15 Predicted Raman bands of C/O models: (a) - 8:1 (400-1700 cm^{-1}) and (b) - 8:2 (400-1600 cm^{-1}) 42

Fig. 4.16 Predicted Raman bands of C/OH model (8:1) (400-3700 cm^{-1}).....42

Fig. 4.17 Raman spectra of an 8.33 mg/mL mixture of graphene platelets with water on a Si substrate (50-4000 cm^{-1}).....43

Fig. 4.18 Raman spectrum of dried graphene oxide solution on an Au coated glass slide (100-4000 cm^{-1}) 44

Fig. 4.19 Raman spectra of a 25 mg/mL solution of fullerenol ($C_{60}(OH)_{24}$) in water on Si (100-2000 cm^{-1}) 45

Fig. 4.20 Optical microscopic image of yeast cells in solution on glass substrate 48

Fig. 4.21 Raman spectra of yeast cells with YPD media (900-1900 cm^{-1}).....49

Fig. 4.22 Baseline extracted Raman spectra of yeast cells with YPD media from Fig. 4.21 50

Fig. 4.23 Baseline extracted and normalized Raman spectra of yeast cells with YPD medium (800-1900 cm^{-1}) 50

Fig. 4.24 Comparison of Raman spectra for yeast cells in YPD medium and cell-free YPD on Si wafers (800-1900 cm^{-1}) 51

Fig. 4.25 Comparison of Raman spectra for yeast cells in YPD medium with fullerenol added, and cells in YPD medium on Si wafers (800-1900 cm^{-1}).....52

Fig. 4.26 Raman spectra of yeast cells in YPD medium on Au-coated glass coverslip and Si wafer with band assignments (800-1800 cm^{-1}).....54

Fig. 4.27 Optical microscopic image of HeLa cells on a glass substrate.....56

Fig. 4.28 Raman spectra of HeLa cells with L-15 medium and L-15 medium alone (700-1900 cm^{-1}) 57

Fig. 4.29 Baseline-extracted and normalized Raman spectra of HeLa cells with L-15 medium and L-15 medium alone on glass coverslips with band assignments (700-1800 cm^{-1}).....58

Fig. 4.30 Comparison of Raman spectra of HeLa cells with and without a 20 nm Au layer on the substrate (800-1800 cm^{-1}) 59

Fig. 5.1 Raman spectrum of a single yeast cell on an Ag nanoparticle substrate using a 514.7 nm laser.....6

Fig. 5.2 Comparison of Raman spectra for yeast cells (top) and HeLa cells (bottom), and their respective media. The vertical translucent bars highlight bands for which similar shifts were observed in the two cultures. Blue bars mark bands that exhibit similar relative intensities, whereas green bars mark bands that are pronouncedly different in relative intensities 64

1. INTRODUCTION

Nanotechnology, nanoscience and biological sciences are innately interconnected since basic functional units of biological systems, such as proteins, membranes, or nucleic acids, represent complex nanoscale objects [1.]Nanoscale imaging and nano diagnostics are in incredible demand because of a promise of a greater sensitivity and earlier detection, and ultimately improved chances of cure, of many diseases such as cancer, and cardiovascular diseases [2,3]. In medical applications, the usage of one of the most promising nanomaterials, nanostructured gold (Au), goes back to ancient times [4]. In the recent years, the usage of plasmonic gold nanoparticles as biological probes already has enriched biological sensing to a greater extent [5]. Further, a broad range of novel bio detection methods using silica nanoparticles, quantum dots, magnetic nanoparticles, or microtubules have also progressed toward many applications such as cell labeling, cell tracking, *in vivo* imaging, magnetic resonance imaging (MRI), DNA detection, or small molecules detection [1,6]. In chemical and biological imaging, various types of vibrational spectroscopies, such as infrared and Raman spectroscopy, have a vast potential [7].

The main reason of the interest in using the Raman spectroscopy is that Raman spectra provide a structural 'fingerprint' of analyzed molecules [8]. Furthermore, surface-enhanced Raman spectroscopy (SERS) allows for a high sensitivity when Raman-active molecules are located close to roughened noble metal surfaces [9,10,11,12]. Due to the inert nature and biocompatibility of gold, Au nanostructures are particularly often used for the SERS enhancement [13]. Raman spectroscopy and SERS have already been instrumental in applications to nucleic acid-based detection, immunoassay-based analyte detection, entire

cell detection, and tissue analysis [14]. SERS is highly regarded for ultra-sensitive applications down to single molecule analysis, both for *in vivo* and *in situ* applications in various industries.

In this work, protocols for Raman spectroscopy of liquid biological samples were optimized. Raman spectra of two different cell cultures, yeast cells and HeLa cells, were collected using several substrates, and interpreted. The potentiality of SERS enhancement was tested for both yeast and HeLa cell cultures on substrates coated with an Au layer. To facilitate the interpretation of collected Raman spectra, less complex water-soluble carbon based materials such as graphene oxide and fullerenol also were characterized, and the results were compared with predictions of the density-functional theory. These studies have demonstrated a proof-of-principle Raman characterization of living cell cultures. My results suggest their spectral band assignments, elucidated differences and similarities in Raman bands of the two cell cultures and finally, achieved a pronounced SERS enhancement for HeLa cells.

2. LITERATURE REVIEW

2.1 Probing of Biological Materials at the Nanoscale

Nanotechnology, nanoscience, and biological sciences are inherently interrelated since basic functional units of biological systems, such as proteins, membranes, and nucleic acids, represent complex nanoscale objects [1]. Ongoing advancements in nanomaterials science are expected to be of transformative significance in many areas of biomedical research and development, including genomics, proteomics, tissue engineering, and regenerative medicine. For example, nanomaterials are very promising for the diagnosis, treatment, monitoring, and control of diseases [15,16]. Nanomaterial based medical products approved by the Food and Drug Administration (FDA), and are currently in various stages of clinical trials, ranging from anti-cancer drugs to antibacterial hand gels or heart tissue regeneration products [17]. However, translation of nanomaterials from the laboratory to the clinic is still early in the pipeline.

In a recent Materials Research Society (MRS) Meeting in San Francisco of 2015, scientists from different regions discussed the identification, development, synthesis, and utilization of nanomaterials, which fall into three broad categories: nanotherapeutics, imaging and diagnostics, and tissue regeneration. Gold nanoparticles, polymeric nanoparticles, liposomes, and carbon-based nanomaterials in particular are highly regarded as a platform for diagnostic and therapeutic applications [6].

Nanoscale imaging and nano diagnostics are in tremendous demand due to a promise of a greater sensitivity and earlier detection, and eventually improved chances of cure of many diseases such as cancer cardiovascular diseases [2,3]. The use of biosensors

with an ability to provide fast and accurate detection of diseases, reliable imaging of cancer cells, molecular-level monitoring of angiogenesis and cancer metastasis, and accurate determining of the effectiveness of anticancer chemotherapy agents, promises a vast potential [18]. In the food industry, nano materials are also in high demand, especially in relation with the detection of pathogens, pesticides, and other contaminates of food before packaging and distribution [19].

Medical applications of one of the most promising nanomaterials, nanostructured gold (Au), go back to ancient times [4]. However, confirmed efficacy of gold treatments dates from 1934, when an application of gold to treatment of arthritis was reported [6]. Since 1950s, colloidal suspensions of Au particles were used as radiotracers for sentinel lymph nodes mapping [20]. Moreover, Au was also demonstrated to attenuate high-energy radiation such as X-rays, which enabled usages of gold particles as a tracer or contrast agent for radiology [21]. Currently, precisely engineered and optimized Au nanostructures are extensively used for numerous diagnostics and therapeutics applications, primarily due to their inherent bio inertness and tunable optical properties [20]. In particular, the usage of plasmonic gold nanoparticles (AuNPs) as biological probes already has enriched biological sensing to a great extent [5].

Numerous nanomaterials were found useful for imaging and diagnostics purposes. In the past few years, a wide range of novel bio detection methods employing silica nanoparticles, quantum dots, magnetic nanoparticles, or microtubules have been developed toward many applications such as cell labeling, cell tracking, *in vivo* imaging, magnetic resonance imaging (MRI), DNA detection, cell detection including circulating tumor cells and tissues, and small molecules detection [1,6]. For example, magnetic nano

particles are useful as contrast agent for MRI and in drug delivery tracking [3]. *In vivo* fluorescence imaging techniques employ semiconductor quantum dots. When quantum dots are covalently attached to biomolecules, they demonstrate a superior brightness in comparison to organic dyes and fluorescent proteins, a property useful for cells or tissues imaging [3,22]. Dye-doped silica nanoparticles represent a different kind of emerging optical imaging agents, which can provide intense fluorescence signal orders of magnitude greater than single organic fluorophores. This material also exhibits a high emission intensity, excellent photo stability, water solubility, and an easily alterable surface [3,22].

In chemical and biological imaging, various types of vibrational spectroscopies also have a vast potential. For example, an emerging coherent Raman scattering microscopy was found useful to detect cell apoptosis based on a selective imaging of CH_2 and CH_3 vibrations in lipids and proteins in organelles of the cell [7]. This spectroscopy also has a potentiality in mapping spatial and temporal dynamics of drug molecules with fluorescent labeling. A different vibrational method, stimulated Raman scattering microscopy, can be used to monitor cell cycle according to a selective imaging of DNA using the signal from C-H vibrations. Such spectroscopies also proved to be suitable for *in vivo* imaging of skin [7].

2.2 The Raman Effect

Raman spectroscopy is a vibrational spectroscopic technique, which involves inelastic scattering of monochromatic light by molecules. Unlike elastic Rayleigh scattering, in Raman effect, frequency of the scattered photons is either decreased or increased in comparison with the original monochromatic frequency (Fig. 2.1) [8]. The

information about vibrational, rotational, and other motions in molecules can be gathered from these frequencies shift. Raman spectroscopy is complementary to the infrared (IR) absorption spectroscopy, with the difference that IR bands result from absorption of photons by molecules, whereas the Raman scattering involves a significantly faster excitation of virtual states in the molecule, resulting in frequency shits of the scattered light [23]. Despite a difference in selection rules, Raman and IR spectra often contain similar bands. Raman spectroscopy is extensively used in materials identification, chemical analysis and characterization since it was discovered in 1920s by C.V. Raman and K.S. Krishnan [24]. The main reason of the interest is that Raman spectra provide a structural 'fingerprint' of analyzed molecules [25]. However, the Raman effect is a relatively weak process. Cross-sections of Raman scattering are between 10^{-31} and 10^{-29} cm^2/molecule in most cases [26].

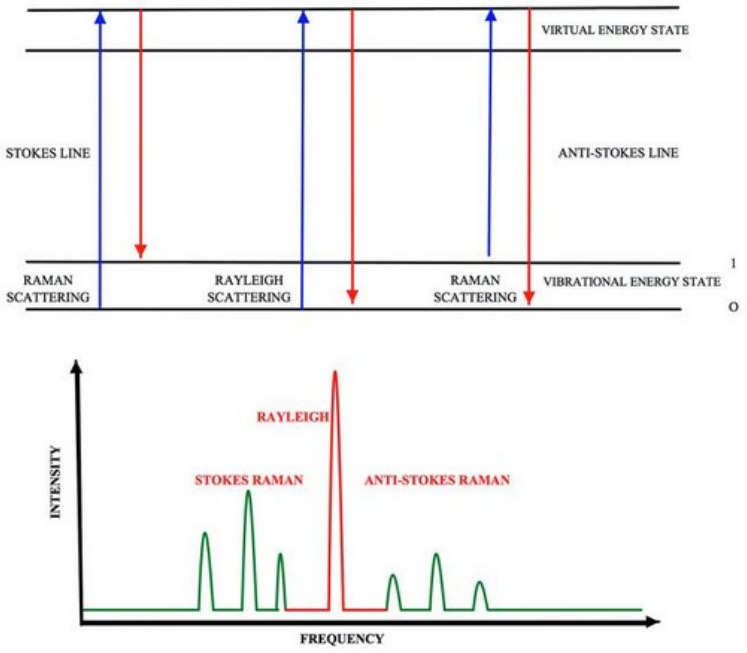

Fig. 2.1 Energy level diagram of Raman and Rayleigh scattering; reproduced with permission of Royal Society of Chemistry [27]

2.3 Surface Enhanced Raman Spectroscopy (SERS)

About 40 years ago, surprisingly strong Raman spectra of pyridine on a roughened silver surface were observed. However, at that time the reason of the enhancement was not known. Later it was recognized that the Raman scattering of light by molecules could be enhanced on roughened metal surfaces [28]. From the time of its discovery, the surface enhanced Raman spectroscopy's (SERS) utilization and interest in it have grown dramatically, demonstrating its potential as an analytical tool for a sensitive and selective detection of molecules adsorbed on noble metal nanostructures [29]. The tremendous amount of published research proves the usefulness of SERS for both fundamental and applied studies in the fields of chemistry, physics, material science, surface science, nanoscience, life sciences, and forensics studies[30,31 ,14,32].

In brief, SERS provides information about molecular vibrations by virtue of Raman scattering, which is strongly enhanced when Raman-active molecules are located close to roughened metal surfaces [9,10,11,12]. In the literature, the enhancement of Raman scatterings in SERS is explained in two different ways: I) as an electromagnetic enhancement (EME), which is related to localized surface plasmon resonance (LSPR) on nanostructured metal surfaces exposed to light [33]; and II) as a chemical enhancement (CE), which is associated with charge transfer interactions between the molecule and the metal surface [33,34,35]. LSPR involves resonant oscillations of conduction electrons generated as a result of the interaction of light wave with the surface of metallic nanoparticles (NPs) smaller than the incident wavelength (Fig. 2.2) [36,37]. This interaction leads to the plasmonic oscillations confined around the NPs with a frequency which

significantly depends on size, shape, material, dielectric properties, and particle-particle separation distance of the NPs [13],[37].

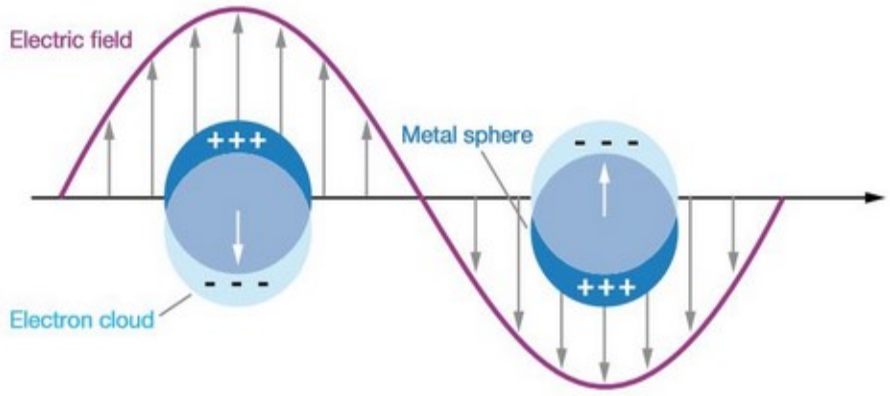

Fig. 2.2 A scheme of localized surface plasmon resonance; reproduced with permission of Annual Reviews [37]

The LSPR is responsible for creating of so-called "hot-spots", or areas of strongly enhanced electromagnetic field on the surface of a NP. The generation of hot spots is often observed around of sharp edges, or in thin gaps between NPs [38]. Molecules located in the hot spots experience a significant enhancement of their Raman scattering cross section, which sometimes even makes it possible detecting single molecules [38].

Although the surface enhancement can make SERS orders of magnitude more sensitive in comparison with the regular Raman spectroscopy, the potential of SERS was not entirely realized until very recently. Early SERS systems suffered from limited reproducibility owing to imperfection of substrates employed [39]. Demonstration of single-molecule SERS detection in 1997 [40], followed by recent advances in nanofabrication, have caused an explosion of new research and transformation of SERS from an interesting physical phenomenon into a robust and effective analytical technique [9,10,11,12]

2.4 Plasmonic Materials

The success of SERS depends strongly on the interaction between adsorbed molecules (analyte) and the surface of plasmonic nanostructures (substrates). Fig. 2.3 shows a schematic of surface enhanced Raman spectroscopy of biopolymer analytes adsorbed on the surface of metal nanostructures.

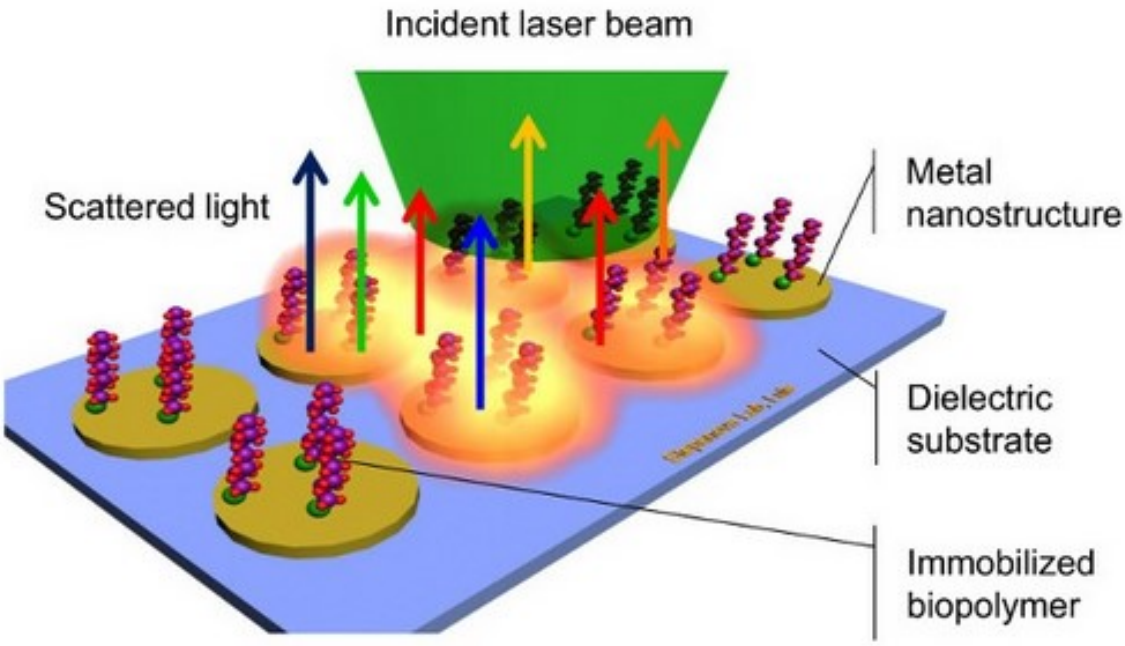

Fig. 2.3 Scheme of surface-enhanced Raman spectroscopy; reproduced with permission of JoVE [41]

Most SERS substrates involve gold (Au) or silver (Ag) nanostructures as they are abundant in free electrons, which creates favorable conditions for the creation of plasmonic hot-spots, in turn resulting in an increase of the Raman intensity. Furthermore, these two metals, and also copper (Cu), have LSPR-related absorption bands covering most of visible and near-infrared wavelength regimes, where most Raman excitation sources function (Fig. 2.4) [42]. Due to the inert nature and biocompatibility of gold, Au nanostructures are particularly often used for SERS enhancement [13].

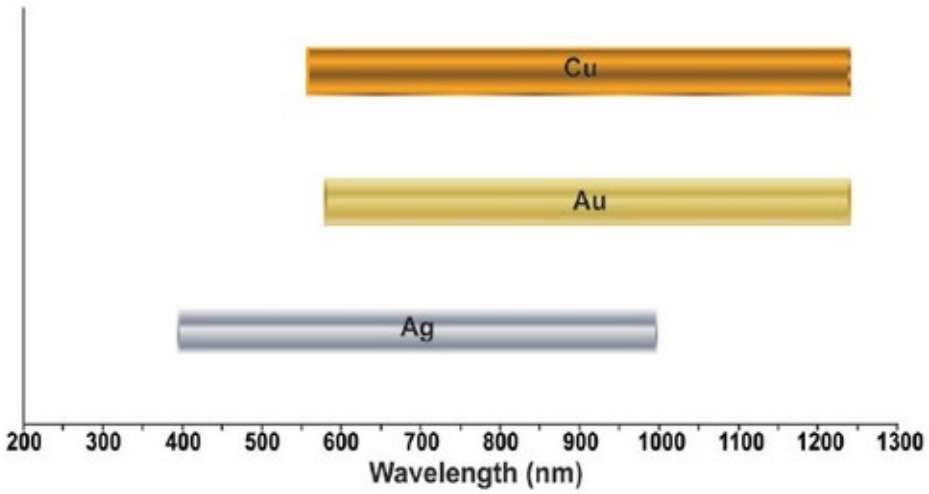

Fig. 2.4 Approximate wavelength ranges where Ag, Au, and Cu nanostructures show LSPR absorption of light; reproduced with permission of Elsevier [42]

2.5 Applications of Raman spectroscopy and SERS

Raman spectroscopy and SERS have several advantages over other bio-analytical methods. These include, first of all, their inherent molecular specificity against unlabeled analytes, and relatively narrow spectral bands. Importantly, water exhibits few Raman bands, allowing minimizing the background signal in biological solutions. Furthermore, SERS has an extremely high sensitivity. Raman spectroscopy and SERS have already been instrumental in applications in nucleic acid-based detection, immunoassay-based analyte detection, entire cell detection, and tissue analysis [31]. SERS is also highly regarded for applications down to single molecule analysis, both for *in vivo* and *in situ* applications in various industries. One example is the recent progress in the development of sensors of glucose, which is important to control diabetes[43]. In this application, a silver film on a surface of nanospheres is functionalized with a decanethiol and mercaptohexanol self-assembled monolayer (SAM) (Figs. 2.5 a, b,c). It was demonstrated [43] that such sensor can precisely measure glucose concentrations in the blood.

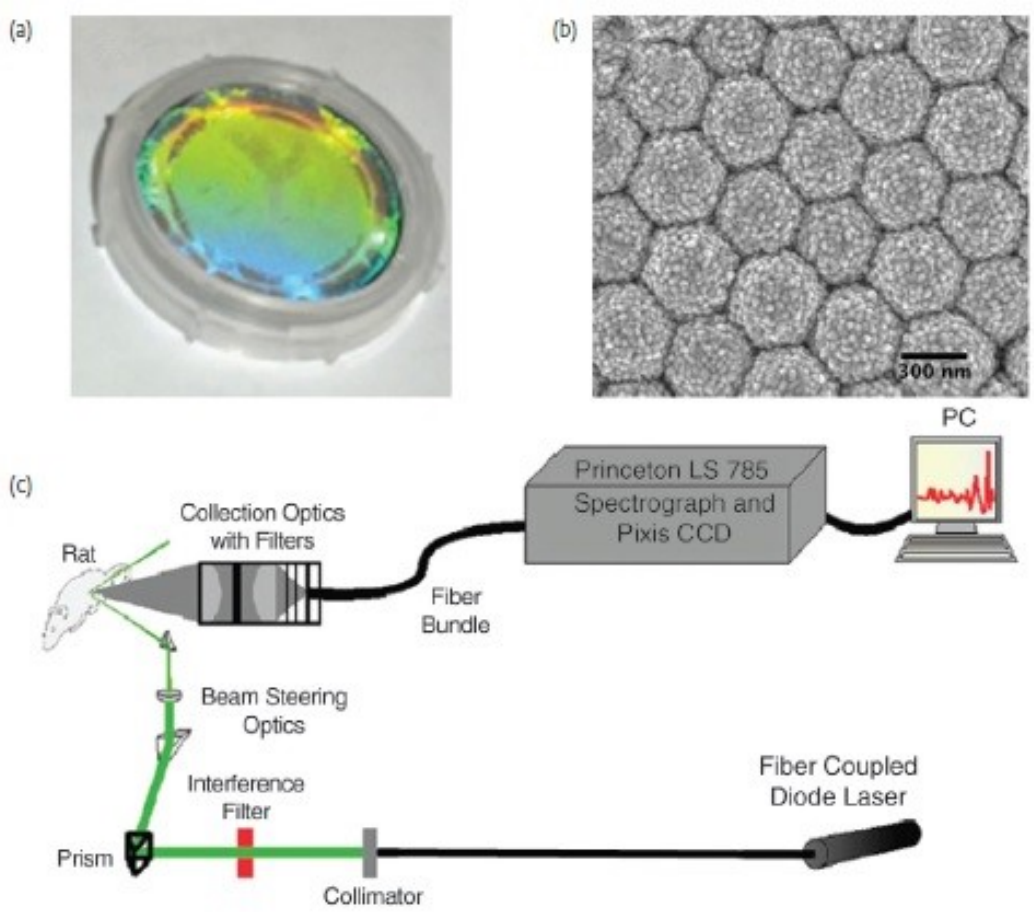

Fig. 2.5 (a) - Silver film (200nm) over 880 nm Si nanospheres (AgFONs) on an 1-inch glass coverslip; (b) - SEM image of the system; (c) - Schematic of the acquisition apparatus; reproduced with permission of Elsevier [43]

Applications of SERS have also been developed for use in conjunction with electrochemistry to monitor the behavior of molecules in different oxidation states[43]. Chemical information was obtained in real-time during a switch of potential for a derivative of tetrathiafulvalene (TTF, Fig. 6), a highly redox-active compound that is highly regarded for applications in mechanostereochemistry and molecular electronic devices [44]. Gold film over nanopsheres (AuFON) was used as a SERS-active electrode in an investigation of structural changes and redox properties of TTF [44]. The SERS spectra of a monolayer of TTF were acquired as a part of cyclic voltammetry measurements (Fig. 2.6). A change in vibrational frequencies as a result of a change in oxidation state is

shown from the results. In addition, as the potential was swept, dramatic changes in signal were observed.

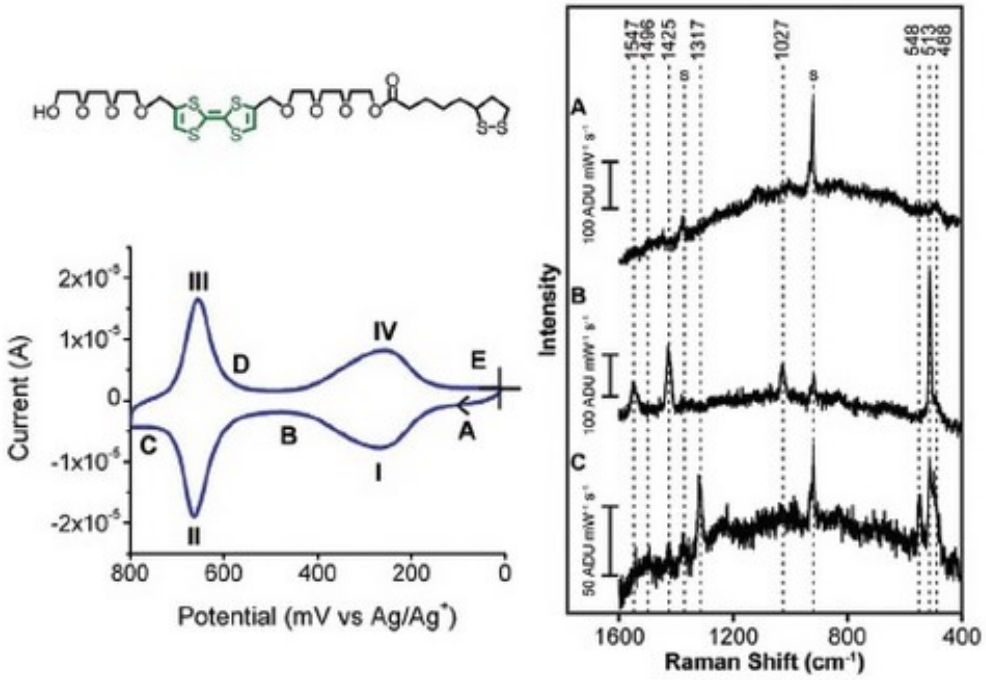

Fig. 2.6 Spectroelectrochemistry of a tetrathiafulvalene -derivative. Top left: molecular structure; bottom left: cyclic voltammogram in acetonitrile on a gold film over nanopsheres; right: surface-enhanced Raman spectra at different potential; reproduced with permission of Elsevier [44]

Single molecule SERS promises substantial advantages in comparison with single molecule fluorescence [30]. Since exploiting extremely large effective cross sections (10^{-16} to 10^{-17} cm^2 per molecule) available from surface-enhanced Raman scattering (SERS), is instrumental for single molecule Raman scattering [45], accurate experimental determination of the enhancement factors is very important. This may be tackled with two recently developed techniques, bi-analyte SERS and temperature dependent SERS vibrational pumping. It was demonstrated that SERS enhancement factors as low as 10^7 are sufficient for the observation of single molecule SERS signals, with maximum single

molecule enhancement factors typically on the order of ~10^{10} [31,42]. Particularly for rapid detection and identification of individual DNA bases, single molecule SERS is a very promising application. In this case, the structural specificity of Raman spectroscopy is used to characterize individual base pairs in DNA fragments without the use of fluorescent labels [46]. It is also possible to distinguish signals that originate from various adsorbates, even at very low concentrations. A well-known example is the detection of SERS vibrational signatures from single molecules of pigment rhodamine 6G (Fig. 2.7)[47].

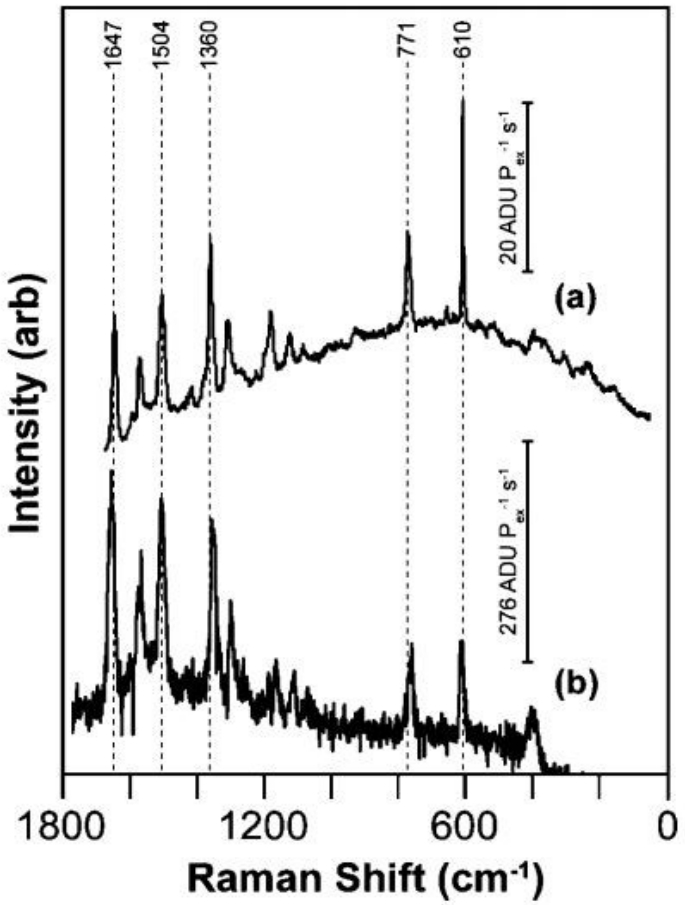

Fig. 2.7 Representative single-molecule SERS spectra of rhodamine 6G on silver obtained using a 532-nm excitation. (a) - Ensemble-averaged SERS obtained on an Ag island film and (b) single molecule SERS spectrum obtained on a colloidal Ag aggregate; reproduced with permission of Elsevier [47]

Due to their advantages, Raman scattering and SERS are increasingly often used in the detection and diagnosis of various biological samples, including body fluids, entire cells, and tissues. For example, Raman Spectroscopy has already been used a lot for live cell and tissue studies for pharmaceutical and diagnostic purposes. [46,48] In particular, non-invasive and label-free Raman imaging allows for interrogating of cells and tissues under normal physiological conditions. Current applications of live-cell imaging allow differentiating cell types [46,52]. Many kinds of disease markers, including cancers, diabetes, inflammation, Alzheimer's and Parkinson's diseases, and others, may be detected using Raman or SERS biosensors, which is important for both biomedical research and clinical diagnostics of the future [49,50]. One example is examining differences between normal and cancerous cells. Certain proteins are found only in cancer cells and not in normal cells of the same phenotype, and detection of such proteins may aid in the diagnosis of disease [49,50,51]. SERS is also highly regarded as a platform for DNA gene detection using nanostructured metallic substrates as SERS-active platforms, and employing DNA sequences complementary to the target DNA as recognition elements[52].

Raman spectroscopy is also very promising for analyzing of foods and drinking water. It has been demonstrated useful for detection of several food components (proteins, carbohydrates, vitamins, minerals, and lipids), pathogens (micro-organisms and viruses), food additives, toxins and chemicals, etc. [53,54]. These applications benefit from such properties of Raman spectroscopy at its material-sensitivity: non-destructive nature, high speed, and independence on pre-treatment steps and labelling. [27]

2.6 Project Goals and Objectives

The main goal of this research work was to optimize the protocols for Raman spectroscopy of liquid biological samples, and demonstrate applications of these protocols to the characterization of live cell cultures.

Specific objectives of the work comprise:

- Development of experimental protocols and procedures for preparing samples of live cell cultures for Raman characterization;
- Collection of Raman Spectra of various liquid samples, mainly the live cell samples;
- Comparative analysis of various settings of the Raman microscope and identification of optimal settings for the biodetection;
- Comparative analysis of Raman bands of the cell cultures on different substrates, as well as of functionalized graphene compounds;
- Tests of potential SERS enhancement when characterizing the cell cultures on substrates containing a plasmonic-active layer.

3. METHODS

3.1 Instruments

3.1.1 Light Microscope. The light microscope is a common research instrument that employs visible light and magnifying lenses for detecting small objects, which are not visible to the naked eye [55,56,57]. In this project, a Motic AE31 inverted biological microscope (Fig. 3.1) was used to visualize HeLa cells and capture images of the cells using the LAS EZ microscope camera software.

Fig. 3.1 The Motic AE31 inverted biological microscope [58]

3.1.2 Fluorescence Microscope. Fluorescence microscopy is a useful tool in the fields of biology, biomedical sciences, and materials science because of its sensitivity and specificity. It has great potentiality in the studies on detecting living cells, and also helps elucidating the structure and functionality of the cells by introducing fluorescent probes or dyes, such as fluorophores or fluorochromes, into the living cells. The method is

capable of detecting weak fluorescent signals from living cells, and even can detect individual molecules. [59]

In this study, a Zeiss Axio Observer A1 fluorescent microscope is used, which consists of AxioCam MRm monochrome digital camera and three different objective lenses: 10X, 40X and 63X. The software ZENworks used along with this powerful microscope allows capturing cells images and videos. The image (Fig. 3.2) was taken using this fluorescent microscope which shows HeLa cells in the Leibovitz's L-15 medium.

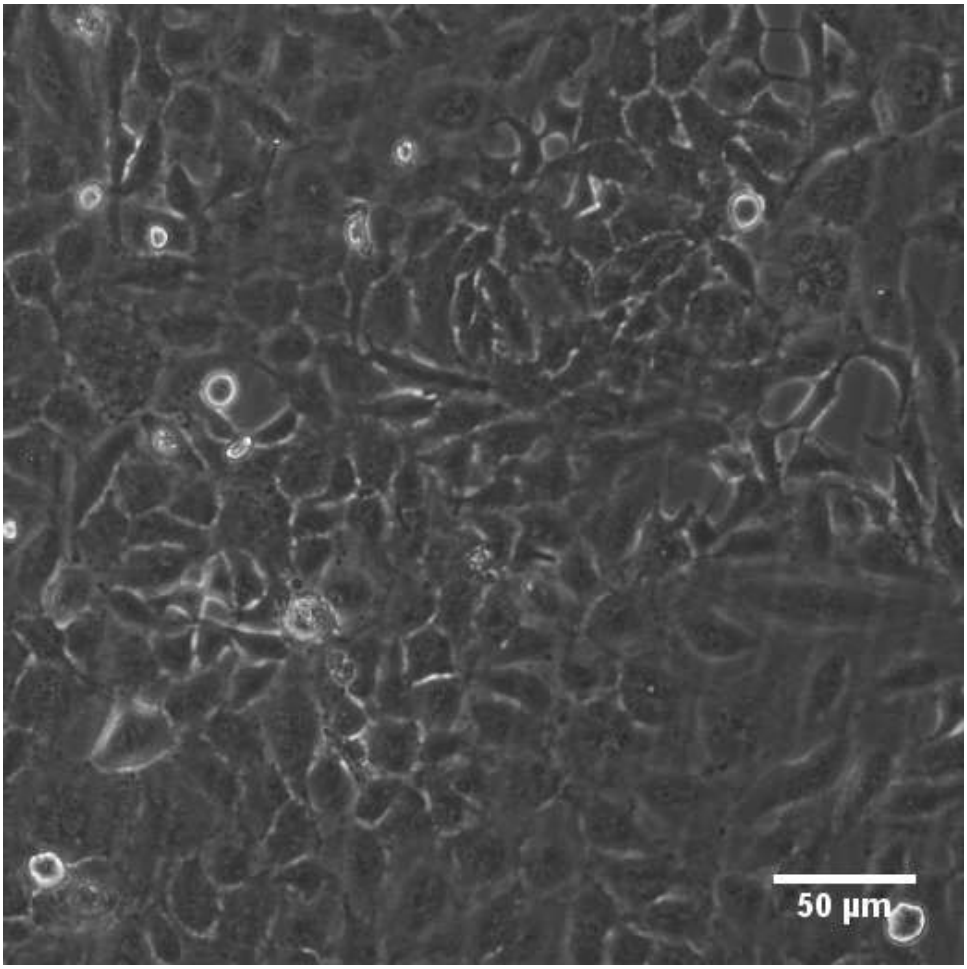

Fig. 3.2 Fluorescent microscopic image of HeLa cells

3.1.3 Raman Spectroscopy. The LabRAM HR 800 (Laboratory Raman High Resolution) (Fig. 3.3) system from HORIBA Jobin Yvon Scientific is used in this study. The focal length of this system, which is the distance between the dispersing grating and the detector, is 800 mm. allowing for a high spectral resolution down to 0.3 cm^{-1}. This system has two detectors. A silicon based multichannel array charge coupled device (CCD) detector works with three lasers of 325, 532, and 785nm excitation wavelengths, and operates at -70° C, allowing for a detection of the Raman spectra from UV to near infrared regimes in a single acquisition chain. It is complemented by an indium gallium arsenide (InGaAs) detector operating at -110° C and working with a 785 nm laser. The InGaAs detector allows extending sensitivity spectral acquisition into the IR regimes beyond 1 μm wavelengths. The two complementary detectors make the instrument suitable for analyzing weak Raman shifts in broad wavelengths regimes [60]. The system has a motorized stage that allows for horizontal XY mappings allowing for a dual scan acquisition mode. The autofocus option allows automatically finding the best focus on non-flat surfaces. The optical system is equipped with four diffraction gratings with the groove densities varying from 150 grooves/mm through 2400 grooves/mm. Higher groove densities correspond to a higher spectral resolution [60,61,62.]

Fig. 3.3 LabRAM HR micro-Raman instrument [60]

Our LabRam system is equipped with three lasers, a 325 nm laser (UV laser), a 532 nm laser, and a 785 nm laser. For UV laser, once the power supply is on, it takes less than 10 minutes to turn the laser on. It is not adjustable and the power is kept at a level of 30-35 mW. It is recommended that the UV laser is on at least 30 minutes before switching the power supply off. In case of the 532 nm laser, once the switch of the power supply is turned on, it takes 3-5 seconds to turn the laser on. This laser is adjustable. For example, the current (determining the intensity) can be changed, with maximum attainable power around 80-85 mW. Finally, for the 785 nm laser, it takes 2-3 seconds to turn the laser on. The power of the laser may be varied from 100 mW to 220 mW [61,62]. For all the lasers, there are two main optical filters which block the high-intensity Rayleigh scattered laser light, and allow for inelastically scattered light to pass through the spectrometer and detector [63]. In this work, 532 nm laser is used along with its corresponding 532 nm bandpass filter (BPF) and 532 edge filter (EF) to pass frequencies within a certain range and reject others. The 532 nm BPF allows to pass only a desired narrow range of frequencies with a transmission of >90% [64], whereas the 532 nm EF absorbs all wavelengths up to 534 nm and transmits those above 534 nm [63].

To visualize the results of Raman imaging measurements, the LabSpec 5 software was used. This is a very efficient and user-friendly tool for researchers and analytical operators. It allows generating Raman spectra and maps with different system settings.[61]

3.1.4 Fume Hood. Laboratory fume hood is a ventilation device intended to provide personnel protection against hazardous airborne components, such as fumes, vapors or dust, Fume hoods also protect against and other chemical spills contaminations [65]. In this work, a fume hood was used to culture HeLa cells, which is shown in Fig. 3.4.

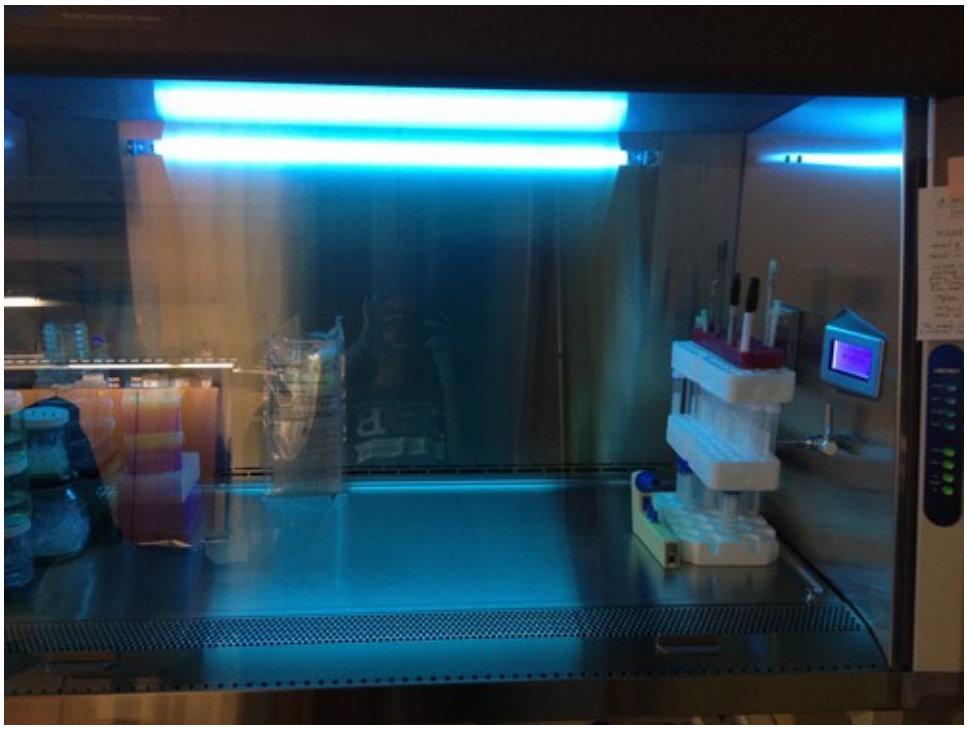

Fig. 3.4 Fume hood

3.2 Simulation and Visualization Software

3.2.1 Quantum ESPESSO. Quantum ESPRESSO (opEn-Source Package for Research in Electronic Structure, Simulation, and Optimization) is an Open-Source computer code for electronic-structure calculations, and ab initio quantum chemistry and materials modeling at the nanoscale. It is mainly based on the Density-Functional Theory (DFT), and employs the plane-wave pseudopotential method [66].

In this work, the Quantum ESPRESSO software package was used to calculate Raman bands in selected materials. The electron–electron interactions were treated using the gradient-corrected Perdew–Burke–Ernzerhof (PBE) exchange-correlation functional for norm-conserving pseudopotentials. The kinetic energy cutoff employed for plane-wave expansion of electron wave functions was set to 100 Rydberg (Ry) and the charge density cutoff was 160 Ry. The Brillouin zone (BZ) integration was sampled on a grid of

2x2x1 k-points, and the convergence threshold energy was 10^{-7}, whereas the mixing factor for self-consistency was equal to 0.7000 [67,68,69], meaning that at each iteration,70% of new density result was mixed with 30% of old density result to have a faster convergence. Structural parameters were relaxed using the Broyden-Fletcher-Goldfarb-Shanno (BFGS) minimization method. The structure was relaxed until the energy change was less than 10^{-4} Ry, or the force was less than 10^{-3} Ry/au [70].

3.2.2 VESTA. VESTA (Visualization for Electronic and STructural Analysis) is a 3D visualization system that has been developed to visualize both structural models, electron or nuclear densities, wave functions, and electrostatic potentials [71,72,73], as well as crystal morphologies [74]. In this work, the VESTA package was used to visualize selected molecular structures.

3.3 Cell Cultures

3.3.1 HeLa Cell Cultures. The HeLa (ATCC CCL-2) cells were cultured in accordance with protocols adopted in the laboratory of Dr. Paul Durham at the Department of Biology of the MSU. The cells were grown inside T-15 flasks, immersed in 5 mL of Leibovitz -15 (L-15) glutamine media supplemented with a 10% fetal bovine serum (FBS) solution and a 1% penicillin streptomycin (PenStrep) solution at 37° C in a humidified atmosphere. All the components were purchased from either from Sigma Aldrich or from Fisher Scientific. Cells were fed by replacing of the L-15 medium solution with a fresh supply every alternative day. Growth of the cells was observed using the light microscope 48 hours after each medium replacement.

To split the cell cultures, the old medium was aspirated off from the flask, and the cells were washed off with 500 µL of phosphate-buffered saline (PBS) of 7.4 pH. After rinsing the flask thoroughly, PBS was aspirated off, and 500 µL of a solution of enzyme trypsin in ethylene diamine tetra acetic acid (EDTA) was added in the flask to break down proteins that keep the cells adherent to the surface of the flask, so that the cells could be detached. After trypsinization for 5 minutes, the cells were observed with the microscope to confirm that they were detached from the surface of the flask. Afterwards, 4.5 mL of L-15 medium solution was added to the flask. The FBS contained in the solution quenched the trypsinization. Then, the medium solution was pipetted up and down, and squirted around the interior of the flask to remove any remaining adherent cells from the surface. The final step was to mix the cell stock from the old flask with a fresh L-15 solution in a clean T-15 flack. Cells were split in several proportions, such as 1:2 (2.5 mL of new medium solution added to 2.5 mL of old stock), 1:4 (3.75 mL of new medium solution added to 1.25 mL of old stock), 1:5 (2.5 mL of new medium solution added to 2.5 mL of old stock), and 1:8 (4.4 mL of new medium added to 0.625 mL of old stock), depending on the requirements. After the splitting process, cells were incubated at 37 °C in a humidified atmosphere.

3.3.2 Yeast Cell Cultures. The cultures of *Saccharomyces* cerevisiae cells described below were prepared by John Short from Dr. Kyoungtae Kim laboratory at the Department of Biology of the MSU. Broth cultures were grown in a standard yeast extract peptone dextrose (YPD) medium, which is a complete medium for yeast growth containing yeast extract, peptone/tryptone, and dextrose solution in deionized water (DI). 1 mL of YPD broth consists of 10 µL yeast extract, 20 µL tryptone, and 20 µL dextrose,

in DI. To grow cell samples, YPD was inoculated with cell stock from a 4˚ C storage and incubated overnight at 30˚ C with shaking. The doubling time of the cell strain under such conditions was approximately 90 minutes. Several kinds of samples were prepared: basic yeast cell cultures in YPD medium; cell cultures in YPD medium with fullerenol treatment; cell cultures in a 2% dextrose solution in DI water; and control samples containing YPD media without cells. Fullerenol solutions were added to the samples in concentrations of 5 µg/mL, 10µg/mL and 20µg/mL, and then incubated for an hour at 30° C with shaking. Cells in pure dextrose solutions were first grown in YPD as described above, then centrifuged for 5 min at 2000 rpm (revolutions per minute), the supernatant was removed and the cell pellet was resuspended in a 1 mL DI by vortexing. The procedure was repeated twice, after which the cells were resuspended in a 1 mL of a 2% solution of dextrose in DI. The optical density of the cell samples at a 600 nm wavelength (OD_{600}) was measured using a Thermo Scientific Biomate3 spectrophotometer.

4. EXPERIMENTAL DESIGN AND RESULTS

4.1 Raman Spectroscopy of Liquid Samples

Distinct from inorganic materials, most biological samples require an aquatic environment to be stable or functional. In this research work, one of main challenges was to optimize protocols for collecting Raman spectra of liquid samples with the LabRam HR 800 instrument. Extensive help of Dr. Robert Mayanovic from Department of Physics, Astronomy, and Materials Science, and Dr. Sergey Mamedov from HORIBA Scientific, was instrumental for the success of this part of the work, and the author would like taking this opportunity to thank them for their support during my journey through this work. In this section, the experimental setup developed for collecting Raman spectra of liquid biological samples is described, and the corresponding optimized experimental protocols are explained. An example of Raman septum of a biological sample is given, and the procedure adopted for processing of raw Raman data is outlined. The experimental setup, the protocols, and the data processing steps described here have been followed in other sections of this chapter to process the corresponding experimental data.

4.1.1 Laser and Microscopic Objectives Selection. For this work, the 532 nm laser has been selected. In general, the excitation wavelength, the accessible laser power, and the linewidth are the most important parameters for selecting a laser for Raman spectroscopy. According to the literature[75], the Raman scattering efficiency is higher for shorter wavelengths as more scattered photons are produced; however fluorescence from the sample also increases, which can immerse the Raman signal. Specifically for applications to biological samples such as cell cultures, a better tradeoff of the Raman

scattering signals and the fluorescence is achieved at 532 nm excitation wavelength in comparison to lower wavelength lasers [76,77]. Another important aspect specific to biological samples is their propensity to degrade when exposed to laser tight. The main reason of the damage is linked to light absorption. From this point of view, near-infrared lasers would produce less photodamage in comparison to visible light ones [76,77]. Although a 532 nm laser has would produce more power in comparison to a longer wavelength laser, in this work I choose the 532 nm laser as it gives a better signal intensity from the samples with less background noise compared to the 785 nm laser.

Another very important factor is the laser's power. In this work, a typical laser intensity used was about 4.39 $mW/\mu m^2$ at the 532 nm excitation wavelength. The optimal power P was calculated based on the magnification, the laser spot size (D) and the numerical aperture (NA), which characterizes the solid angle of light collection, using the formula below based on the Rayleigh criterion for diffraction-limited resolution [78],

$$P\ (mW/\mu m^2) = 25\ mW/\ (\pi * (D/2)^2) \quad (1)$$

$$D = 1.22\lambda/NA,\ \lambda = 532\ nm \quad (2)$$

where 25 mW is the total laser power on the sample.

The selection of microscope's objective lens is also crucial in Raman spectroscopy. The objective lens' throughput depends on its numerical aperture. Objective lenses with high magnification or high NA are deemed suitable for thin-film crystal samples as they provide a higher axial spatial resolution and shorter working distance. However, for transparent biomaterials, somewhat lower magnification and lower NA objectives are preferable as they have longer working distance to avoid the sample touching the objectives, and also provide milder exposure conditions.

In this work, an objective lens with a 10X magnification was used that allows for the smallest numerical apertures, longer working distances, and bigger spot sizes in comparison to other options available in our lab. The usage of low numerical apertures (NA) causes a large spot size of the laser resulting in a lesser power density, which prevents sample of overheating. Table 4.1 lists the available magnification options for the 532 nm laser. The settings used in this work are given in the bottom line of the table. It can be seen that these settings minimize the radiation power on the sample in comparison with the other options.

Table 4.1 Laser power (25mW) calculations for the various magnifications

Magnification	Numerical Apertures	Laser spot size (μm)	Working distance (mm)	Radiation power ($mW/\mu m^2$)
100×	0.90	0.721	0.27	~61.23
50×	0.75	0.865	0.38	~42.54
10×	0.25	2.69	10.6	~4.39

4.1.2 Substrate Selection. Of primary interest for this work were biological samples contained in small amounts on solid substrates. Since most of our substrates were transparent fluids, the material of the substrate was important. Four different substrates were used, such as ordinary glass coverslips; Si wafers; glass coverslips covered with an either 10 nm or 20 nm thick Au layer; and steel slides. Out of these, glass coverslips are the simplest to use in cell culture experiments, whereas Si wafers provide minimal background signal and also facilitate focusing, since they are opaque for visible light. Glass coverslips coated with thin Au films combine these advantages, as the Au film allows for a light scattering sufficient for focusing purposes, while partially

screening Raman bands originating from the glass [75]. Furthermore, 10-20 nm Au films also allow for a SERS enhancement or Raman bands from the sample. The deposition of Au on gold slides was performed by the staff of the Center for Applied Science and Engineering (CASE) at the Roy Blunt Jordan Valley Innovation Center (JVIC). The deposition was done by magnetron sputtering (Emitech K550X) of gold. Prior the deposition, the glass slides were sonicated in acetone and plasma-cleaned (Nordson March Jupiter III).

4.1.3 Experimental Design and Procedures. Fig. 4.1 shows a scheme of the samples used in this work. For example, a glass slide was used to support the substrate. The liquid samples were pipetted on the top of the substrates, forming a droplet as shown in Fig. 4.1. Io collect the Raman spectra; the samples were placed in the LabRAM HR800 instrument as illustrated in Fig. 4.2.

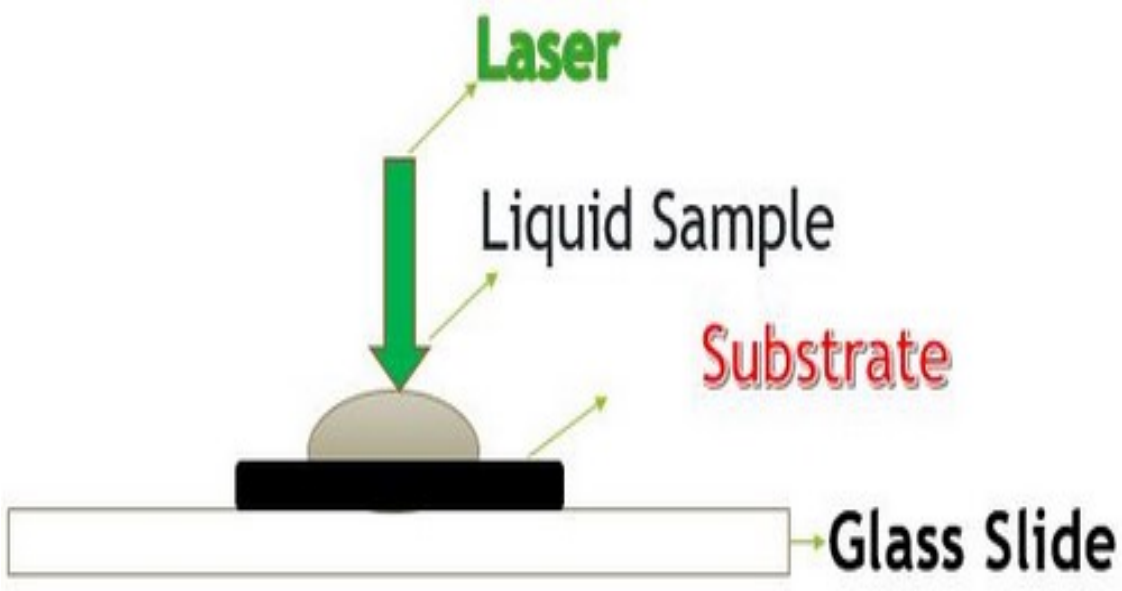

Fig. 4.1 Scheme of experimental setup for collecting Raman spectra of liquid samples

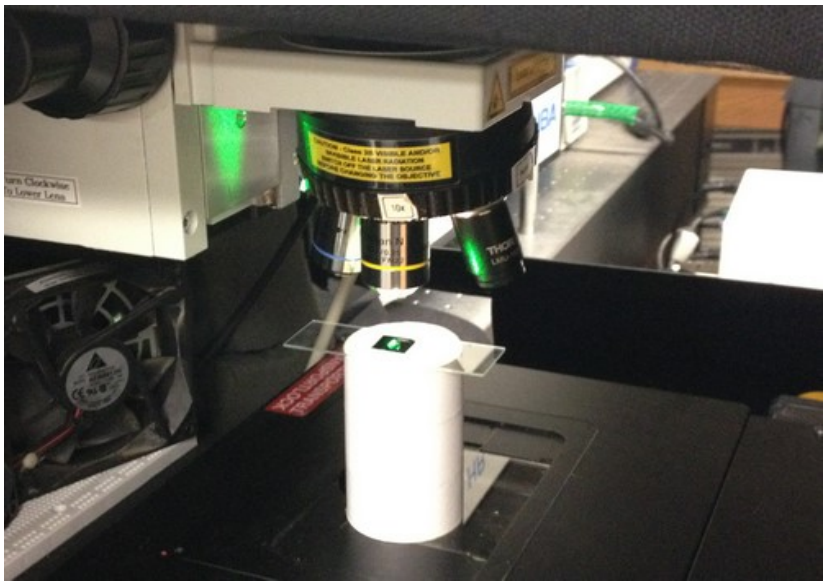

Fig. 4.2 Sample area of the LabRAM HR800 instrument.

During the Raman measurements, the instrument was first calibrated using the easiest reference material, silicon, which has a sharp peak at 520.5 cm^{-1}. To minimize the laser intensity and prevent the damage of biological samples, a 200 μm confocal hole and a 600 grooves/mm grating were used. Different filters were employed, such as D0.1, D1, D2, D3 and D4, with the corresponding levels of passed laser power of 50%, 10%, 1%, 0.1% and 0.01%, respectively. To maximize the signal from the sample, the intensity correction was turned on to minimize the fluorescence. Focusing on the sample was done either from the top surface of the liquid, or from the bottom (substrate's surface). While focusing from the top of the liquid droplet, the focusing was performed from the reflection generated by the laser visible on the monitor. Then, the real time display was turned on, and the position along the Z axis was adjusted to maximize the signal. After finding the position where the signal was maximal, the data was acquired from that position. When focusing from the substrate surface, first the objective lens was brought close to the sample, and once the substrate surface was visible on the monitor, the position along the Z axis was adjusted in the opposite direction to focus on the sample.

For both approaches, once the signal was obtained, the selected position along the Z axis was reset to zero for making it a reference point. Upon selection of a desired spectral range, the acquisition was performed with a minimal exposure time in the range of 25 seconds to 25 minutes, depending on samples in order to avoid damage of the samples.

4.1.4 Examples. Since all samples in this work were water solutions, I started with collecting Raman spectra of pure water. Fig. 4.3 depicts an example Raman spectrum of pure water on a Si substrate (50-4500 cm^{-1}). To collect the spectrum, one drop of water was pipetted on the surface of a silicon wafer, which was placed on a glass slide. I used the exposure time of 20 s and the accumulation number equal to 3. The spectrum in Fig. 4.3 shows pronounced Raman bands around a 3300 to 3500 cm^{-1} region, which is results from O-H vibrations. The bands visible in the lower shift regions (around 800 to 1000 cm^{-1}) are mainly from native oxide on the surface of silicon. Importantly, water shows few peaks in the biologically relevant region between 1000 and 2000 cm^{-1}, so that the background signal in this region is minimal.

Unlike pure water, spectra acquired from most biological samples contain a rich variety of overlapping spectral bands. Not unusually, the raw spectra also included a significant contamination originating primarily from fluorescence. To improve the signal to noise ratio when required, baseline correction was done by fourth-degree polynomial or fifth-degree polynomial using HORIBA Scientific's LabSpec 5 software. After the baseline correction, normalization was performed to facilitate comparison of several spectra. For few spectra with the strongest background noise, a fourth-degree polynomial smoothing option available in the LabSpec 5 was also used to additionally smooth the spectra. However, the use of this option was kept limited to avoid unwanted side effects

of this procedure whenever possible. After processing of the spectra, the Origin graphic software was used to further analyze the data.

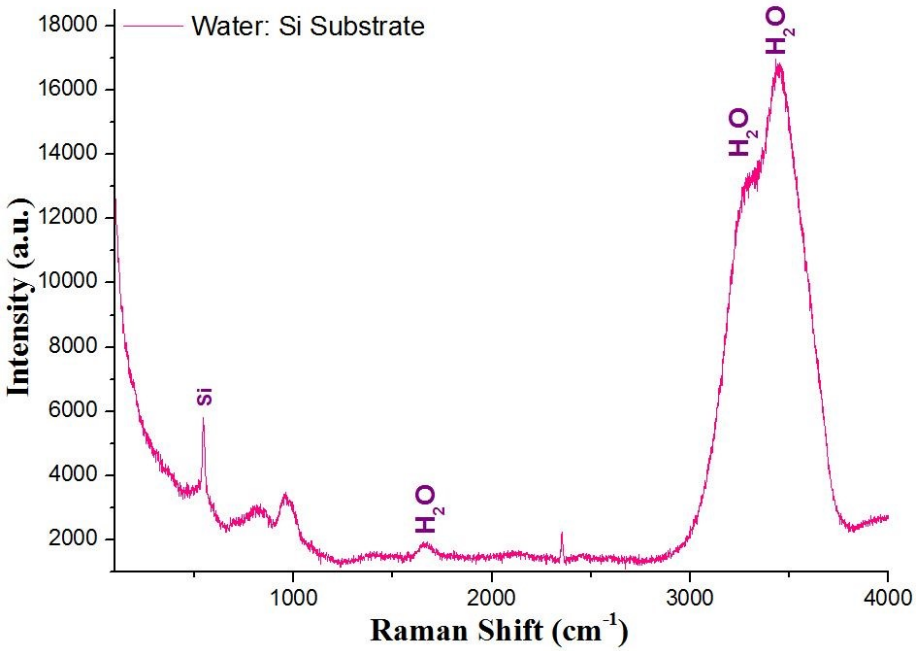

Fig. 4.3 Raman spectrum of pure water on Si substrate (50-4500 cm^{-1})

As an example, Fig. 4.4 shows several raw spectra of a biological sample, yeast extract peptone dextrose (YPD) medium, which was used to culture yeast cells (Sect. 3.3.2). Since the YPD contains an extract from yeast cells, it may be expected to produce complex spectra resulting from many biological compounds. To collect the spectra, four different substrates were used (20 nm Au coated glass coverslips, ordinary glass coverslips, Si wafers, and steel slides). After collecting of the raw spectrum (Fig. 4.4), baseline extraction using a fourth-degree polynomial makes the Raman band much better discernible, as Fig. 4.5 illustrates. The subsequent normalization (Fig. 4.6) helps to compare the different spectra, and interpret the results.

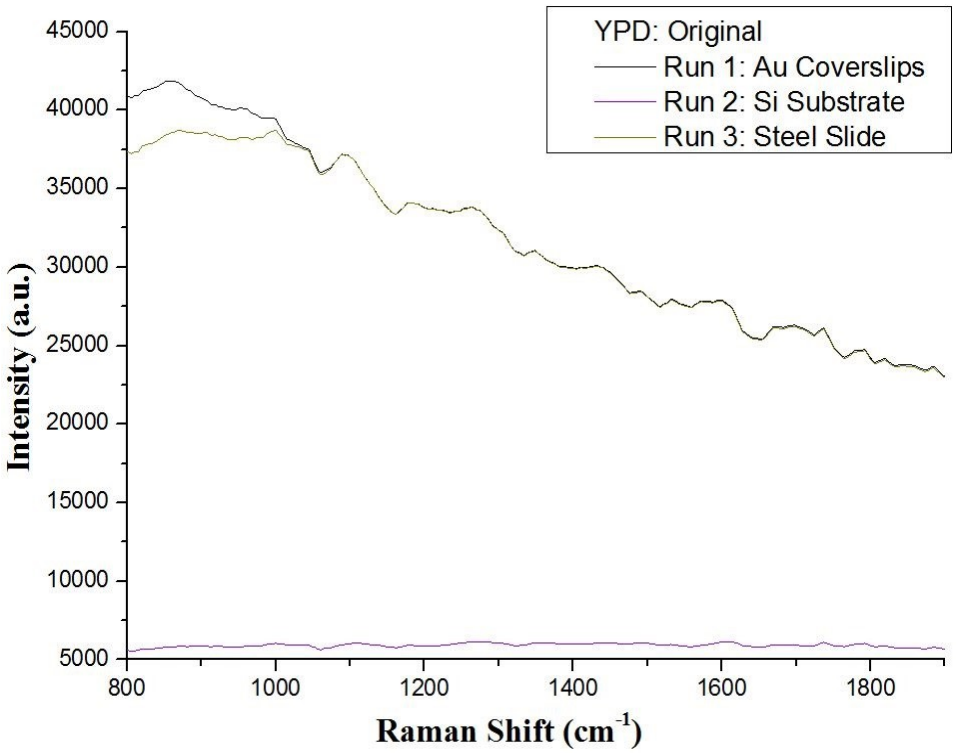

Fig. 4.4 Raman spectra of YPD media (a biological sample) on different substrates (800-1900 cm^{-1})

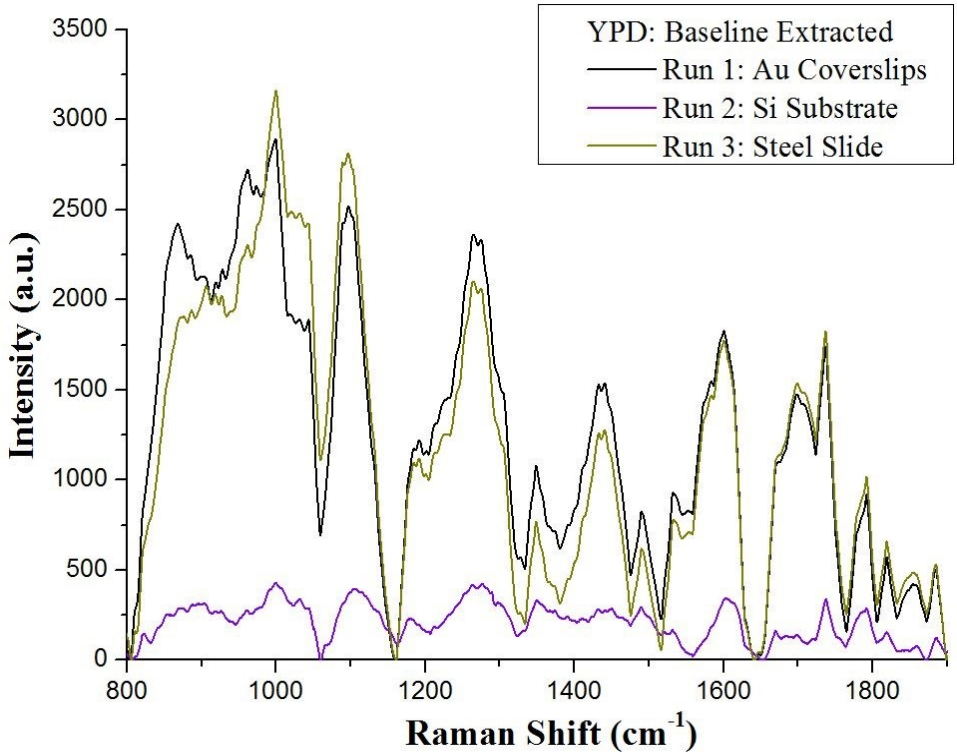

Fig. 4.5 Baseline extracted Raman spectra of YPD media from Fig. 4.4

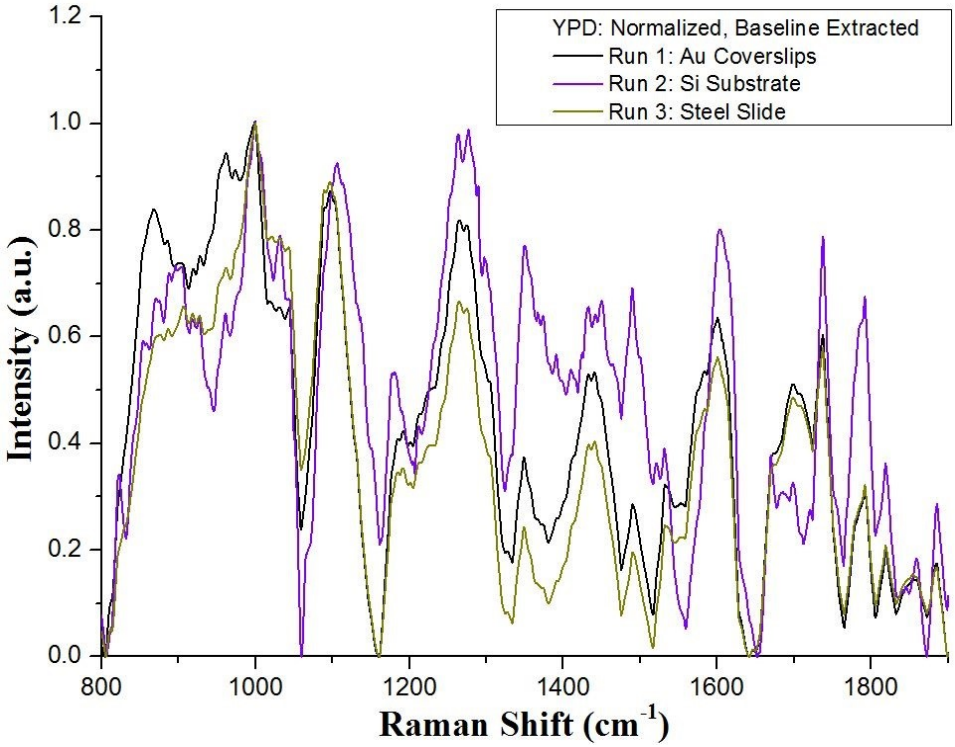

Fig. 4.6 Normalized and baseline extracted Raman spectra of YPD media from Figs. 4.4 and 4.5

4.2 Analysis of Vibrations in Carbon Materials

As the example in Sect. 4.1 illustrates, Raman spectra of biological samples may represent a complex superposition of many bands. In order to facilitate interpretation of Raman bands in complex samples, I have additionally investigated a simpler benchmark example of graphene based materials. Graphene is a two-dimensional crystal comprised of carbon atoms tightly packed into a hexagonal honeycomb lattice. In this study, oxidized graphene was selected primarily for the reason of representing vibrations of C-C and C-O bonds, which are also relevant for many of organic materials. However, graphene and its derivatives are also interesting materials on their own. Graphene structure has unique mechanical, electrical, optical and thermal properties due to its two-dimensional lattice [79,80,81,82,83,84,85], which may adopt many forms known as graphite,

carbon nanotubes, or fullerene [86]. Electronic structure of graphene materials involves sp2 hybridized atoms forming in-plane σ bonds, resulting in a high structural stability. Importantly, delocalization of π bonds out of plane allows for a variety of functional groups to be attached covalently. For example, graphene oxide (GO) may contain hydroxyl (-OH) functional groups [87]. Composition, location, and number of such group may vary. Often, oxidation of graphene is achieved through the intermediate formation of COC (epoxy) groups [88]. In this section, I investigate vibrations of functionalized graphene-based structures both experimentally and computationally using the Quantum ESPRESSO DFT software (Sect.3.2).

4.2.1 Models of Functionalized Graphene-Based Materials. Models of functionalized graphene were built using the VESTA software (Sect. 3.2) A planar graphene structure was constructed from a unit cell of 8 carbon atoms on the xy plane as shown in Fig. 4.7. A vacuum spacing of 20 Å along the z-direction was used to avoid mirror interactions between neighboring images. Oxygen- and hydrogen-containing models (C_8O, C_8O_2, C_8H, C_8H_2 and C_8H_6) as well as a model with OH groups (C_8OH) were prepared. Defects were introduced into by replacing one C atom with O. Fig. 4.8 show a C_7O structure, where a carbon hole was created and replaced by an oxygen atom to model an oxidized graphene structure with defects. The functionalization also included -OH, -H and =O groups, predominantly bound to carbon atoms on the basal plane. All the models of graphene were prepared manually by attaching O, H or OH groups to the C_8 graphene structure using the VESTA software package. In the C/O models, the oxygen atoms were bonded uniformly on the top surface of some selected carbon atoms and the other models such as C/H and C/OH were created by selecting the same carbon atoms to

have a better comparison among all models. The Quantum ESPRESSO DFT code was used to optimize the structures. A 2x2x1 supercell was created using VESTA for better visualization. Figs. 4.9-4.11 illustrate the initial structures (left) and the optimized structures after the relaxation (right).

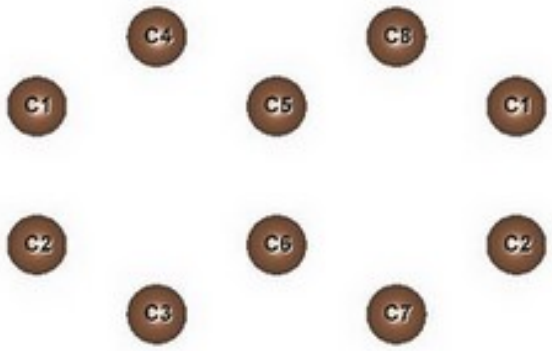

Fig. 4.7 Periodic structure of graphene

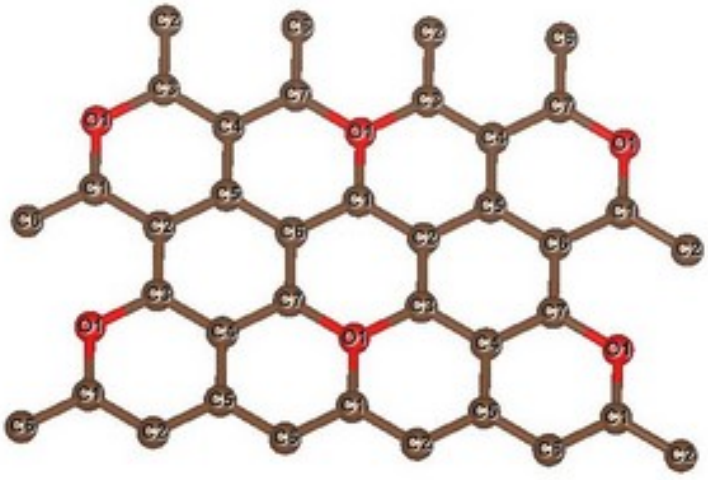

Fig. 4.8 An oxidized graphene structure with defects obtained by replacing C atoms with O atoms. Note that the brown and red lines indicate symmetry of the initial structure, and not actual covalent bonds between the atoms

Fig. 4.9 (a) shows the structure C_8H (8 carbon atoms and one hydrogen atom) where one hydrogen was initially placed on top of one carbon atom. The structures in

Figs. 4.9 (b) and (c) are similar to (a), differing only by the number of hydrogen atoms. The structure C_8H_2 (8 carbon atoms and 2 hydrogen atoms) shown in (b) contains two hydrogen atoms, which were initially placed on top of two carbon atoms. The structure C_8H_6 (8 carbon atoms and 6 hydrogen atoms) shown in (c) contains six hydrogen atoms, which were initially placed on top of six carbon atoms. In addition, the well-known CH_4 model was generated using one carbon atom surrounded with four hydrogen atoms to compare the calculated results with this model.

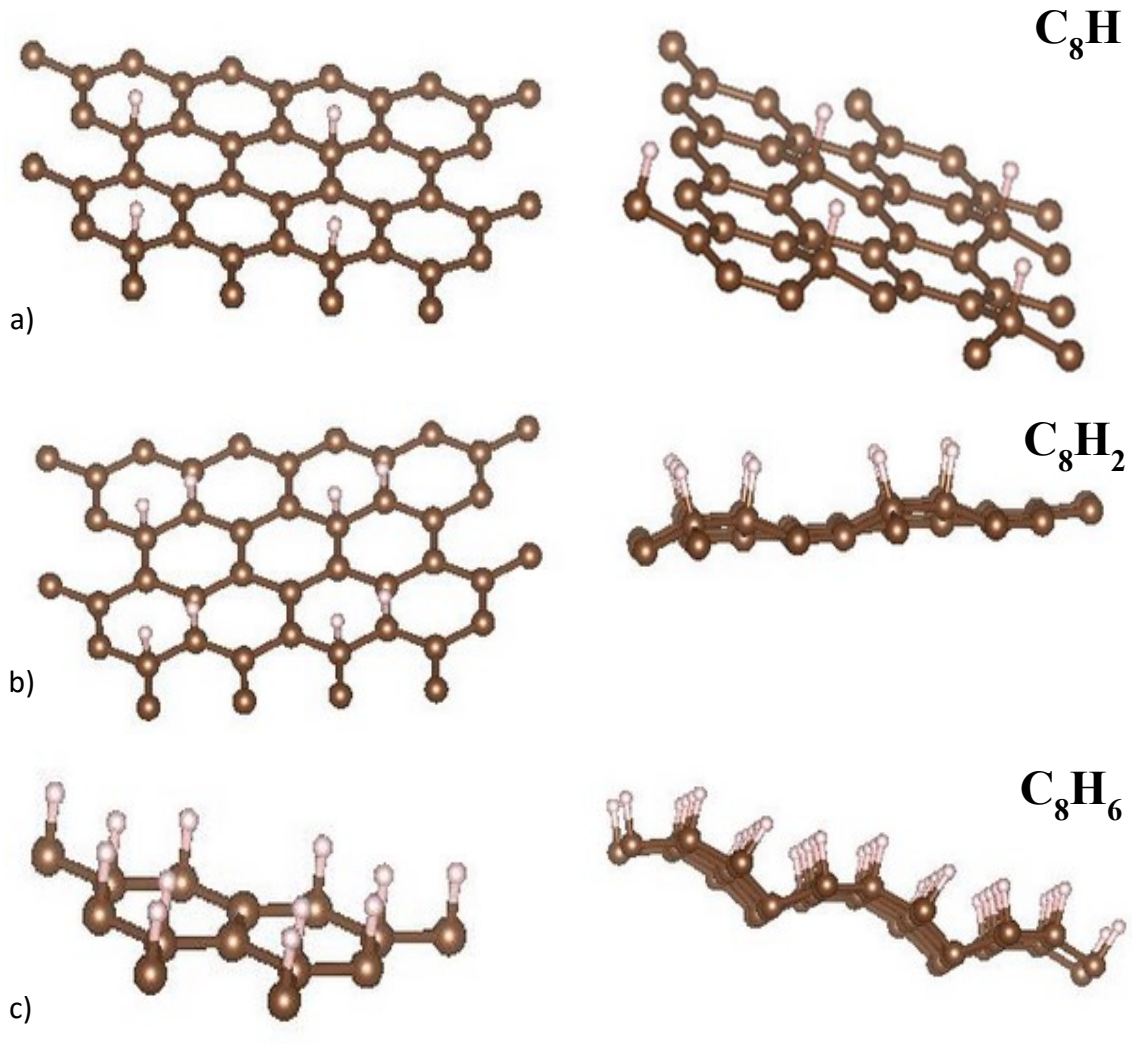

Fig. 4.9 Functionalized graphene with C/H ratios of (a) 8:1, (b) 8:2, and (c) 8:6 before (left) and after (right) relaxation of the structures

Fig. 4.10 (a) shows the structure of C_8O (8 carbon atoms and one oxygen atom), where one oxygen was initially placed on top of one carbon atom, as depicted in the panel on the left. After relaxing of the structure, the oxygen atoms shifted towards the neighbor carbon atoms and formed epoxy-type bonds with two nearest carbon atoms, as in can be seen in the panel on the left. Fig. 4.10 (b) shows the structure C_8H_2 (8 carbon atoms and 2 oxygen atoms), where two oxygen atoms were initially placed on top of two carbon atoms. In this structure, the O atoms remained in close positions after the relaxation.

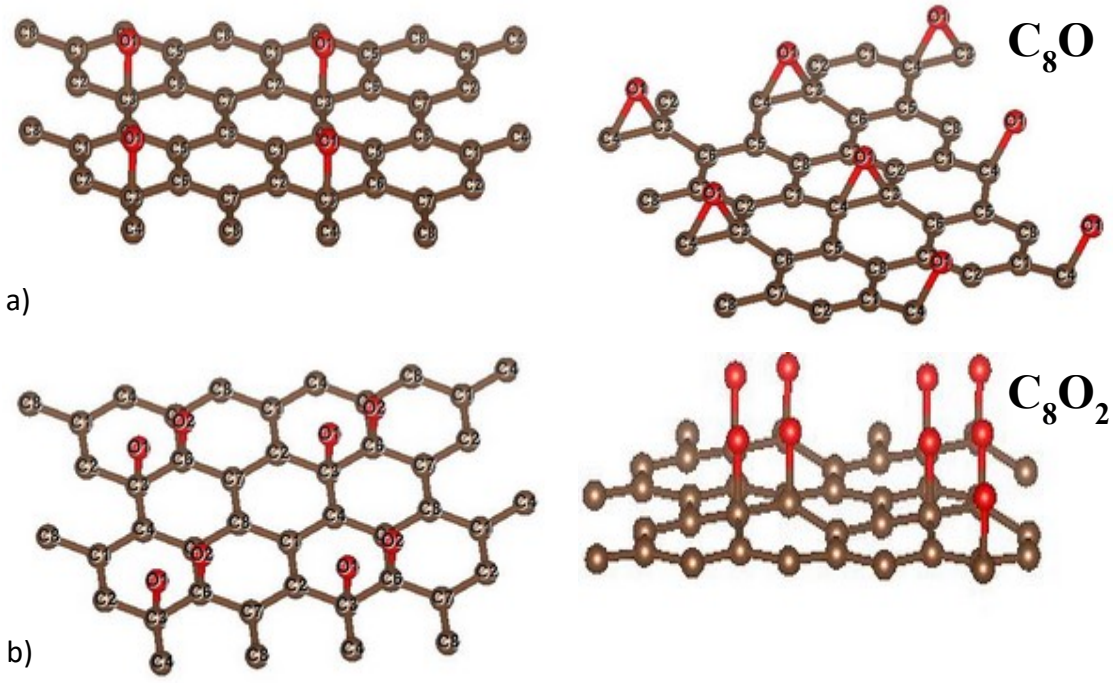

Fig. 4.10 Functionalized graphene with C/O ratios of (a) 8:1 and (b) 8:2 before (left) and after (right) relaxation of the structures

Finally, Fig. 4.11 shows the structure of $C_8(OH)$ (8 carbon atoms, one oxygen atom, and one hydrogen atom). In this case, first, one oxygen atom was positioned on top of a carbon atom, and then a hydrogen atom was attached to the oxygen to create the

initial C_8OH structure shown in the left panel. The panel on the right shows an optimized C_8OH after relaxation.

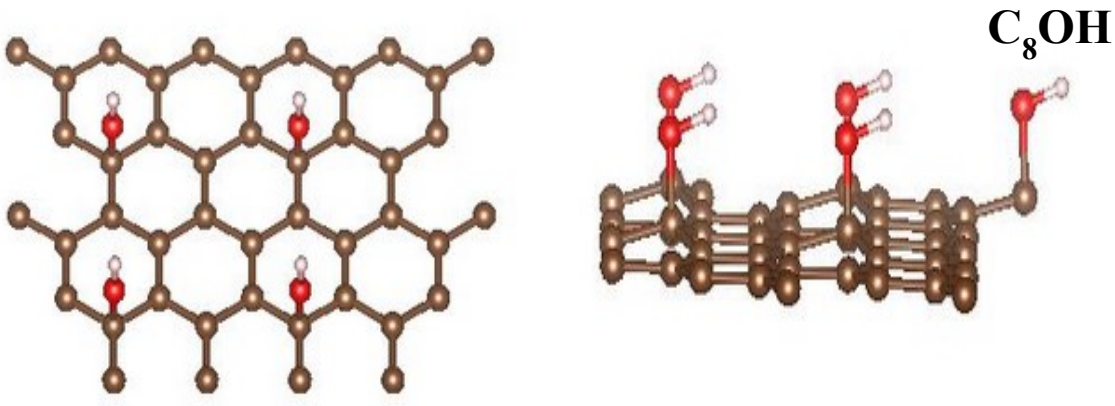

Fig. 4.11 Functionalized graphene with C/OH ratio of 8:1 before (left) and after (right) relaxation of the structure

Tables 4.2 and 4.3 list interatomic distances in the models considered before and after the optimization, respectively. In initial structures before optimization, average C-C distances were equal to 1.418 Å; for C-H and for O-H the distances were 1 Å; and for C-O, they were 1.4 Å (Table 4.2). After optimization of the geometry, vertical displacement of C atoms was observed as Figs. 4.8-4.10 illustrate. In optimized hydrogen-containing models, C-H bond lengths varied from 1.13 Å to 1.10 Å, whereas saturated C–C single bond lengths near H varied from 1.47 Å to 1.52 Å (see Table 4.3). In C_8O due to the oxygen displacement both C-C and C-O bond lengths increased and the oxygen atom formed an epoxy group with two carbon atoms (Fig. 4.10 (a)). However, for system C_8O_2 only a vertical displacement of oxygen atoms occurred (Fig. 4.10(b)). For the C_8OH structure, the plane also was somewhat distorted by the presence of OH groups Fig. 4.11(a)). In this structure, the measured C–O bond lengths was 1.51Å and unsaturated C–C double bonds adopted 1.487 Å lengths.

Table 4.2 Bond lengths for initial 9 structures before relaxation

Graphene Models	C-C Bond Lengths (Å)	C-O Bond Lengths (Å)	C-H Bond Lengths (Å)	O-H Bond Lengths (Å)
C_8	1.417	-	-	-
C_7O	1.418	1.418	-	-
C_8H	1.418	-	1	-
C_8H_2	1.418	-	1	-
C_8H_6	1.418	-	1	-
C_8O	1.418	1.4	-	-
C_8O_2	1.418	1.4	-	-
C_8OH	1.418	1.4	-	1
$C_8(OH)_2$	1.418	1.4	-	1

Table 4.3 Bond lengths for 9 structures after optimizing of the structures

Graphene Models	C-C Bond Lengths (Å)	C-O Bond Lengths (Å)	C-H Bond Lengths (Å)	O-H Bond Lengths (Å)
C_8	1.418	-	-	-
C_7O	1.40	1.46	-	-
C_8H	1.483	-	1.13	-
C_8H_2	1.497	-	1.11	-
C_8H_6	1.4991	-	1.10	-
C_8O	1.46	1.46	-	-
C_8O_2	1.484	1.50	-	-
C_8OH	1.487	1.51	-	0.98
$C_8(OH)_2$	1.417	3.1745	-	0.98

4.2.2 Calculation of Raman Bands in Graphene-Based Materials. The Quantum ESPRESSO code was used to calculate Raman bands of the model graphene-based structures as described in Section 3.2. Figs. 4.12-4.16 illustrate positions of Raman bands obtained for the various structures. Interpretations of the bands were done based on assignments from DFT calculations of comparable structures published in the literature [89,90,91,92 ,93,94,95,96,97,98,99].

Figure 4.12 shows the predicted Raman bands of graphene structure (C_8), where the X-axis represents the Raman shift (cm^{-1}) in the range from 380 to 1650 cm^{-1}. Differently colored bars represent the Raman bands. Raman bands are observed at 383 cm^{-1} and 1091 cm^{-1} are coming from C-C bending; that near 730 cm^{-1} is due to the ring vibration; those near 835 cm^{-1} and 1424 cm^{-1} are due to C–C stretch, and the bands near 1375 cm^{-1} and 1563 cm^{-1} are due to ring stretches.

Raman bands of oxidized graphene with defects (C_7O) are shown in Fig. 4.13. Different colors and bars present different Raman bands in the region from 200 to 1600 cm^{-1}. The figure shows C–C bending bands between 200 cm^{-1} and 510 cm^{-1}, and ring vibration bands at 704 cm^{-1} and 789 cm^{-1}. The band at 928 cm^{-1} has been attributed to the C–O–C group stretch. The band at 1053 cm^{-1} region has been assigned to C–C skeletal stretches. The model also exhibits ring stretch modes at 1362 cm^{-1} and 1589 cm^{-1}.

In Fig. 4.14, panel (a) shows Raman bands of methane CH_4, panel (b) shows Raman bands of C_8H, panel (c) shows Raman bands of C_8H_2, and panel (d) shows bands of C_8H_6. For CH_4, bands are found at 1061 cm^{-1}, 1150 cm^{-1}, 1257 cm^{-1} and 1262 cm^{-1}, and also at 3892 cm^{-1} and 4045 cm^{-1}, however, the bands at 1257 cm^{-1} and 1262 cm^{-1} are overlapped with each other. For C_8H, I observe similar bands as in CH_4, and also many

additional bands between 537 cm^{-1} and 1558 cm^{-1}. For the C_8H_2 and C_8H_6 models, many similar bands have been observed as in C_8H, however, a new band is found at approximately 1630 cm^{-1} for C_8H_6. Several new bands are found in the region between 1630 cm^{-1} and 1930 cm^{-1} and also around 2750 $cm^{-1}$for C_8H_6. In the described hydrogen-containing structures except for CH_4, bands seen between 830 cm^{-1} and 1044 cm^{-1} can be attributed to C–C stretches, whereas ring stretches are observed in the 1325-1568 cm^{-1} region. The bands between 1273 cm^{-1} and 1467 cm^{-1} can be attributed to either C–H or C–C bond vibrations. The models also exhibit higher-order 2D ring vibration bands between 2618 cm^{-1} and 2756 cm^{-1}.

Figs. 4.15 (a) and (b) show Raman band of C_8O and C_8O_2, respectively. In these oxygen-containing structures, the bands in the 400-470 cm^{-1} region are due to C–C bending, and ring vibration bands are observed in the 727-800 cm^{-1} region. The bands in the 850-1070 cm^{-1} region have been assigned to C–C skeletal stretches. Similarly, to the other graphene-based models, ring stretch modes are seen between 1345 cm^{-1} and 1616 cm^{-1}.

Finally, Fig.4.16 shows the Raman bands of the C_8OH structure with OH groups depicted in Fig. 4.10. The C_8OH model shows C–C bending bands between 336 cm^{-1} and 407 cm^{-1} as well as at 1090 cm^{-1}; C–C stretch bands at 835 cm^{-1}, 1044 cm^{-1}, and 1435 cm^{-1}; ring vibration bands around 730-743 cm^{-1}; and ring stretch bands between 1328 cm^{-1} and 1555 cm^{-1}. A 3716 cm^{-1} band is due to hydroxyl groups stretching vibrations.

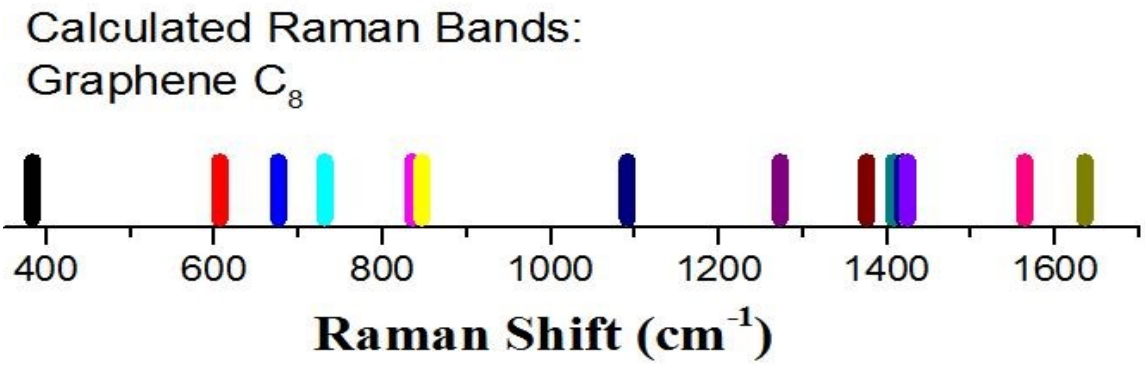

Fig. 4.12 Predicted Raman bands of Graphene (C_8) (300-1650 cm^{-1})

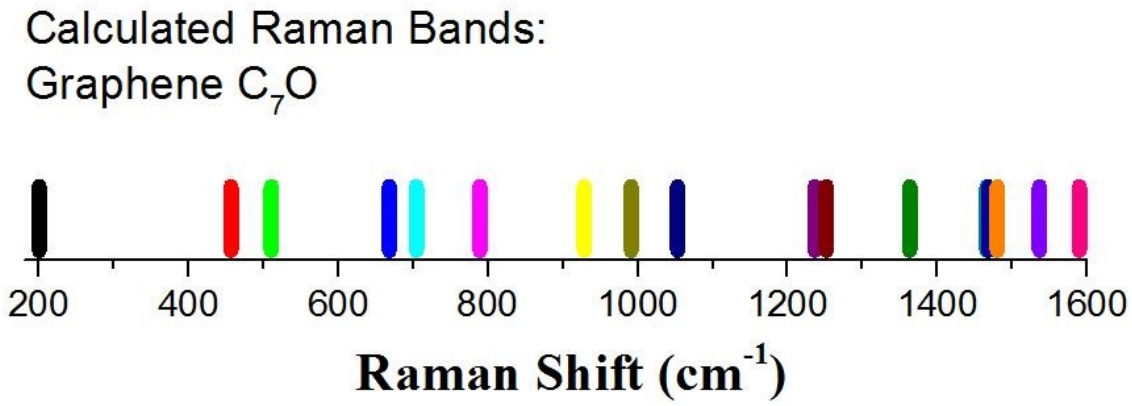

Fig. 4.13 Predicted Raman bands of oxidized graphene with defects (C_7O) (200-1600 cm^{-1})

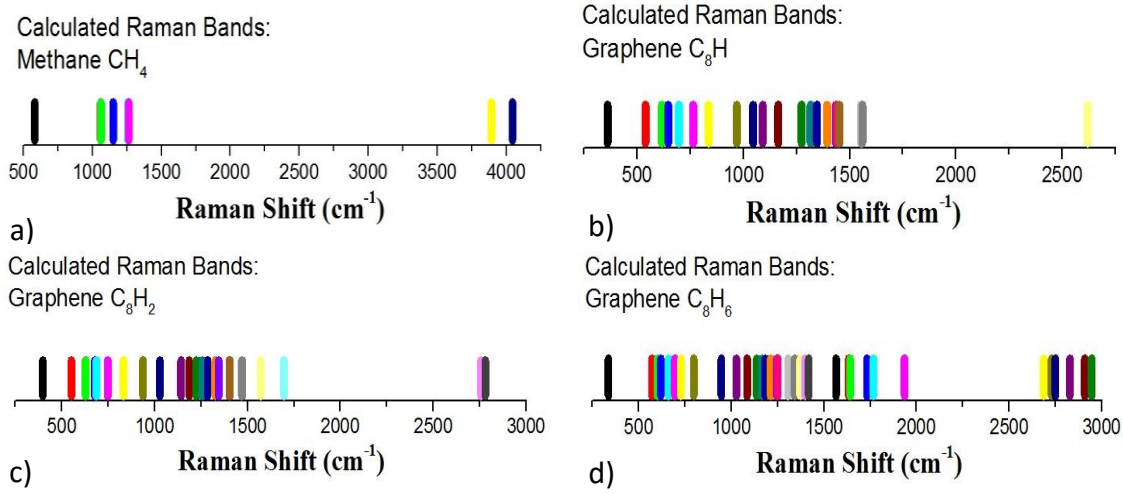

Fig. 4.14 Predicted Raman bands of (a) - CH_4 model (500-5000 cm^{-1}), and (b-d) - C/H models: 8:1 (300-2700 cm^{-1}), 8:2 (300-2800 cm^{-1}), and 8:6 (300-3000 cm^{-1})

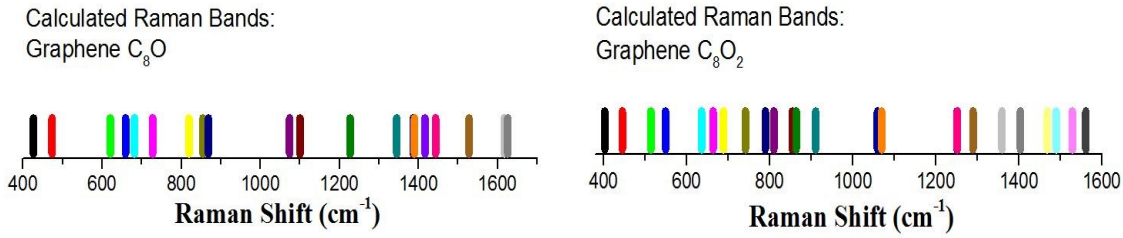

Fig. 4.15 Predicted Raman bands of C/O models: (a) - 8:1 (400-1700 cm^{-1}) and (b) - 8:2 (400-1600 cm^{-1})

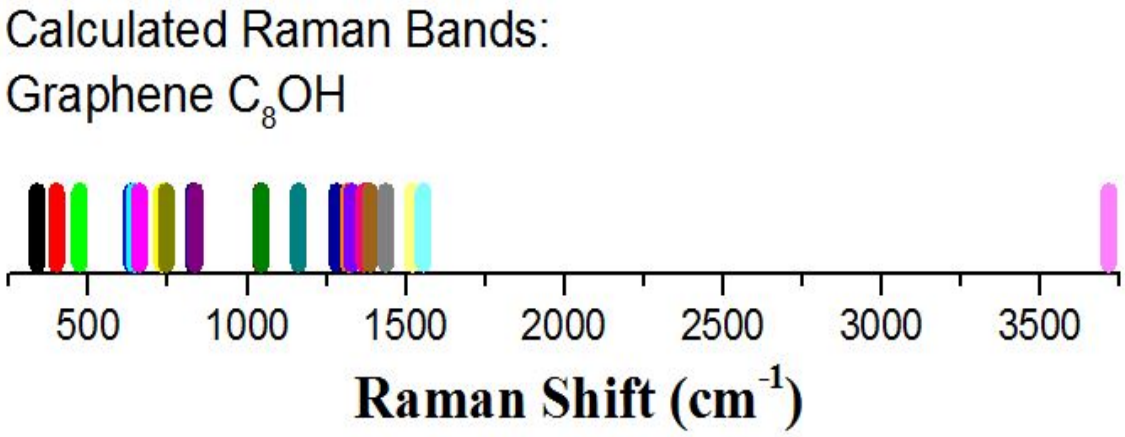

Fig. 4.16 Predicted Raman bands of C/OH model (8:1) (400-3700cm^{-1})

4.2.3. Experimental Raman Characterization of Graphene Oxide and Fullerenol.

Raman spectra were acquired for several graphene derivatives. The samples included oxidized nano graphene platelets mixed with deionized (DI) water; GO solution; and fullerenol ($C_{60}(OH)_n$) solution. 25 mg of oxidized nano graphene platelets in powder form from Angstrom Materials, INC were mixed with 3 mLof DI water to prepare a mixture with the graphene concentration of 8.33 mg/mL. A 2 mg/mL GO solution was purchased from Sigma-Aldrich. Finally, a 25 mg/mL solution of fullerenol (also known as fullerene polyhydroxide) from Materials and Electrochemical Research (MER) Corporation was used as a sample. Raman spectra of the samples were collected as described in Sect. 4.1 using a 532 nm excitation wavelength. The confocal hole size was

kept at 200 µm, and the objective lens had a 10X magnification for all the samples. However, the acquisition time varied from 25 s to 5 min. To obtain spectra of liquid samples, the solutions were pipetted onto a substrate (either a Si wafer or a glass slide with a 10 nm thick Au coating). Alternatively, to obtain spectra of dried samples, the samples were dried using a hot plate, and the spectra were taken afterwards. Lab Spec 5 software was used to collect the Raman spectra and Origin was used to process and analysis all the results as described in Sect. 4.1.4.

Figure 4.17 shows the Raman spectra from water mixture of oxidized nano graphene platelets obtained with the exposure time 10 s and the accumulation number 10. One drop of the mixture was placed on the surface of a silicon wafer, which was in turn placed on a glass slide to collect the spectra. Two spectra have been collected to confirm the accuracy. Baseline correction was subsequently performed using a 5-degree polynomial.

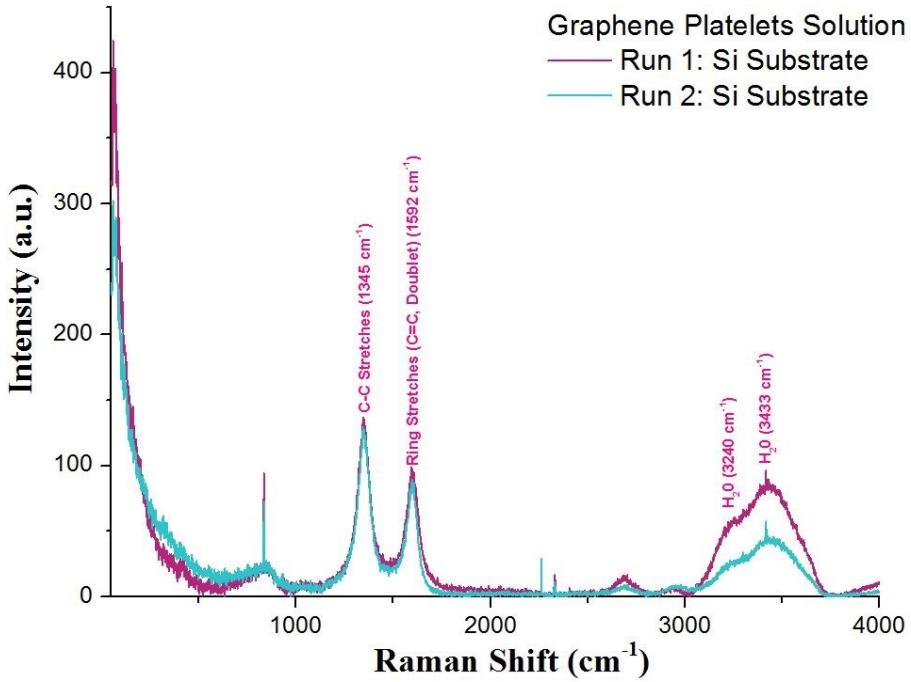

Fig. 4.17 Raman spectra of an 8.33 mg/mL mixture of graphene platelets with water on a Si substrate (50-4000 cm^{-1})

Fig. 4.18 depicts a Raman spectrum of dried graphene oxide. The initial 2 mg/mL GO solution was pipetted onto a glass side coated with a 10 nm layer of gold (Au) and the sample was dried using a hot plate. The Raman spectrum was subsequently taken, the baseline was extracted, and the spectrum was smoothened using a 4-degree polynomial.

Fig. 4.19 represents Raman spectra of a fullerenol ($C_{60}(OH)_{24}$) solution on a Si substrate. To prepare a highly concentrated solution, 25 mg of fullerenol powder was diluted in 1 mL of DI water, which used as a stock for the future experiments. Then, a drop of the solution was pipetted onto a Si substrate. Two acquisition time runs were performed. For the first run the exposure time was 10 s and the accumulation number was 10, whereas for the second run they were 5 s and 5, respectively.

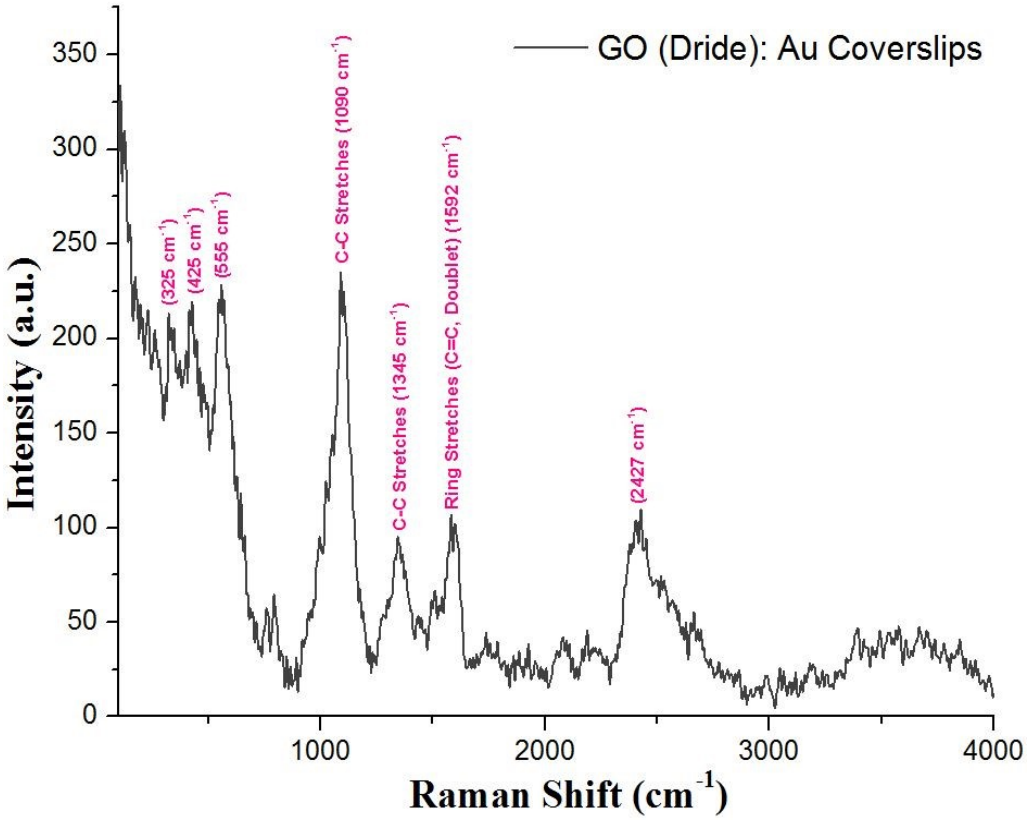

Fig. 4.18 Raman spectrum of dried graphene oxide solution on an Au coated glass slide (100-4000 cm^{-1})

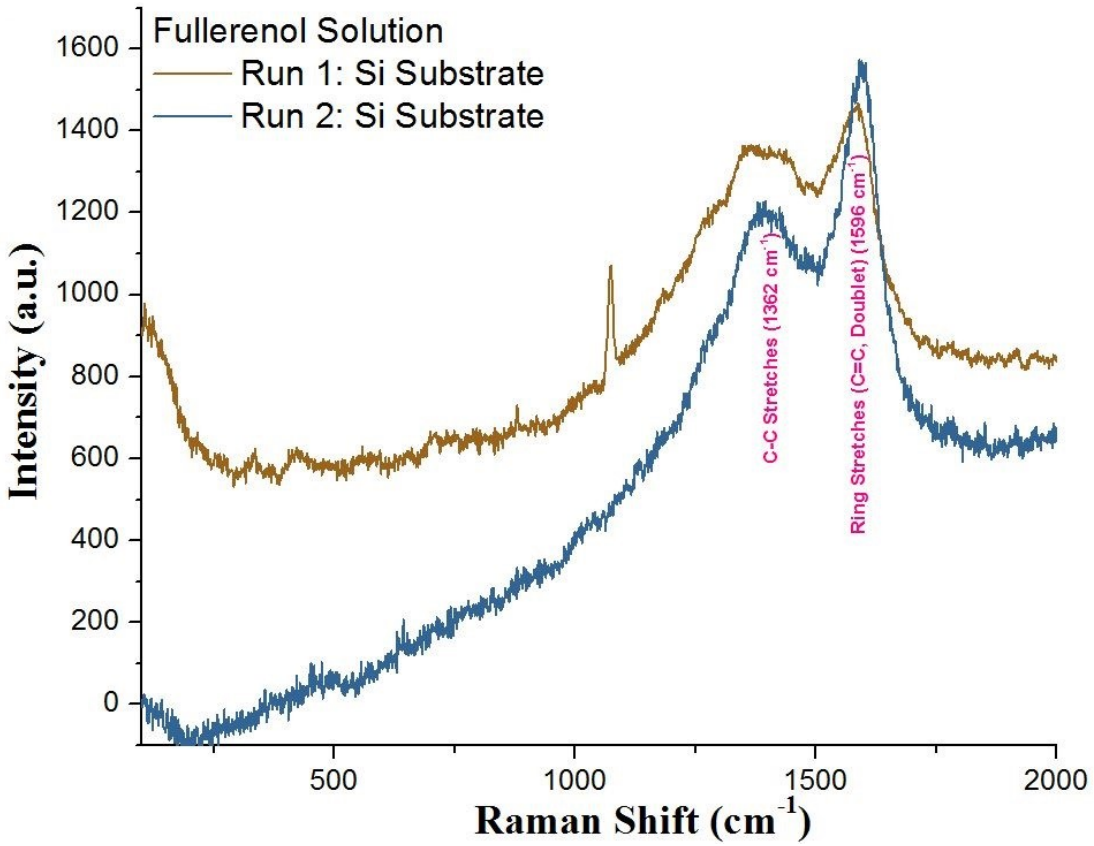

Fig. 4.19 Raman spectra of a 25 mg/mL solution of fullerenol ($C_{60}(OH)_{24}$) in water on Si (100-2000 cm^{-1})

4.2.4. Comparison of Experimental and Predicted Raman Bands. Table 4.4. lists the positions of Raman bands observed experimentally in oxidized nano graphene platelets mixed with deionized (DI) water, dried GO solution, and fullerenol ($C_{60}(OH)_n$) solution. The table also presents the positions of Raman predicted by DFT calculations in the graphene-based models and CH_4. Summarizing the DFT calculations data, most C–C bending and stretch bands fall into 330-1100 cm^{-1} and 832-1074 cm^{-1} regions in the structures considered. C–H vibration bands are found in a narrower region between 1273 cm^{-1} and 1375 cm^{-1}; however, some C–C stretch modes are also found in these regimes. Ring vibration modes are observed between 704 and 796 cm^{-1}, and also at 1325-1616 cm^{-1}. O–H vibration bands are localized at 3716 cm^{-1}.

Table 4.4 Comparison of experimental and predicted Raman bands (cm^{-1})

Band Types [89-99]	Experimental Raman Spectra			Calculated Raman Bands								
	Graphene Platelets with H_2O	GO (Dried)	Fullerenol Solution	C_8	C_7O	CH_4	C_8H	C_8H_2	C_8H_6	C_8O	C_8O_2	C_8OH
C -C Bending	-	1090	-	383 1091	200 453 510	1150	353 1089	397	336 1084	425 473 1074	402 444 1069	336 397 407 1090
Ring Vibration	-	760 794	-	730	704 789	-	761	-	727 796	727	740	730 743
C-C Skeletal Stretch	841	-		835	1053	1061	834 967 1044	832 936 1027	945 1026	854 868 1074	854 863 910 1059 1069	835 1044
C-O-C Stretch	-	-	-	-	928	-	-	-	-	-	-	-
C-H Vibration, C-C Stretch or D-Band	1345	1345 1435	1362	1375 1424	-	1257 1262	1273 1314 1344 1434 1450	1344 1467	1305 1342 1371 1417	-	-	1368 1435
Ring Stretch or G-Band	1592	1592	1596	1563	1362 1589	-	1392 1558	1325 1401 1568 1695	1398 1564 1632 1934	1345 1389 1616	1359 1561	1328 1386 1555
2D Band	2694	2667	-	-	-	-	2618	2756	2685 2749	-	-	-
O-H Stretch	3240 3422	-	-	-	-	-	-	-	-	-	-	3716

In turn, the experimental data of graphene compounds exhibit pronounced bands around 760-794 cm^{-1}, 841 cm^{-1}, 1090 cm^{-1}, 1345 cm^{-1}, 1362 cm^{-1}, 1592 cm^{-1}, and beyond 3000 cm^{-1}. Based on the DFT predictions, the first two sets of bands can be confidently attributed to ring vibration and C–C skeletal stretch, respectively, whereas the band at 1090 cm^{-1} is due to C–C bending. The bands observed at 1345 cm^{-1} and 1362 cm^{-1} have been attributed to C–C vibrations and that at 1592 cm^{-1} is due to ring stretch. The bands of 3240 cm^{-1} and 3422 cm^{-1} observed in the graphene platelets sample arise from O-H bond vibrations.

Specifically, for the spectra in Fig. 4.17, the weak peak observed at 841 cm^{-1} is due to C-C skeletal stretch, and two pronounced bands at 1345 cm^{-1} and 1592 cm^{-1} can be

attributed to C-C stretch and ring stretch, respectively. Two strong bands at 3240 cm^{-1} and 3433 cm^{-1} arise from -OH groups, both from graphene oxide and water.

In Fig. 4.18, Raman bands are observed at the same shifts of 1345 cm^{-1} and 1592 cm^{-1} as in the oxidized nano graphene platelets. Several lower-shift bands are also seen. The bands around 760 cm^{-1} are due to the ring vibration, and the strong band near 1090 cm^{-1} is coming from C-C bending. In Fig. 4.19, the Raman bands found at 1362 cm^{-1} and 1596 cm^{-1} are very close to those observed in oxidized nano graphene platelets and dried GO.

4.3 Analysis of Cell Cultures

In this research work, two examples of biological samples were characterized, live yeast cells samples, and live HeLa cells samples. These examples involve somewhat different processing steps, primarily considering that HeLa cells are cultured on a surface of a substrate (Sect. 3.3.1), whereas yeast cells are grown in solution (Sect. 3.3.2).

4.3.1 Analysis of Yeast Cell Cultures. For the yeast cell cultures, cell stock was grown overnight (Sect. 3.3.2) and Raman measurements were performed after approximately 20 hours so that the cells were highly dense in solution. Most of the time the concentration of yeast cells material, as measured by the optical density method [100], was at the level of 4, or approximately $12x10^7$ cells/mL. Four different substrates were used such as Si wafer, 20 nm Au coated coverslip, ordinary glass slide, and steel slide. Before the Raman measurements, the substrates were washed with a 70% solution of ethanol in water and dried. Subsequently, 60 μL of the YPD medium solution containing yeast cells were pipetted on the surface of the substrates for characterization. Before

collecting Raman spectra, optical microscopic image of the cells was taken to confirm that the cells are present in the solution. An example image of yeast cells in YPD medium is shown in Fig 4.20.

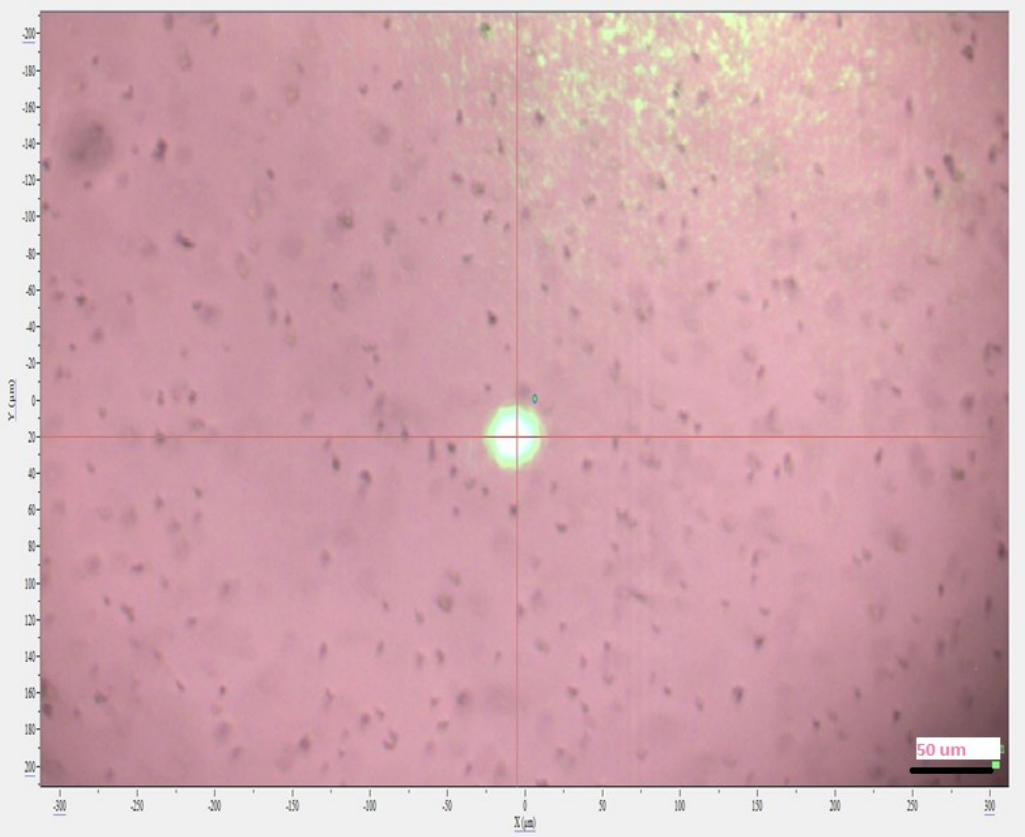

Fig. 4.20 Optical microscopic image of yeast cells in solution on glass substrate

Fig. 4.21 shows raw Raman spectra of yeast cells in YPD medium solution on four different substrates (20 nm Au coated glass coverslips, ordinary glass coverslips, Si wafers, and steel slides). After collecting of the raw spectra, baseline extraction using a fourth-degree polynomial was performed. This makes the Raman bands much easier to analyze, as Fig. 4.22 illustrates. To facilitate comparison of relative intensities of the bands even more, normalization of the spectra was performed such that the intensities of the 999 cm^{-1} band are the same in all the spectra, as Fig. 4.23 represents.

From Figs. 4.22 and 4.23 it is clear that the Raman bands are located at the same positions for all four substrates, indicating that in this case, influence of the substrates on vibrational properties of the sample is minimal. The overall quality of the spectra achieved on bare glass coverslips is inferior in comparison to the other substrates due to unscreened fluorescence and Raman background signal from the glass, as well as due to challenges of focusing onto a transparent sample. Quality of the spectra on Au coated slides is similar to that on Si wafers and steel slides. However, from Fig. 4.21 it appears that Au coating of the glass coverslip does not provide a significant enhancement of the Raman signal of the yeast cell solution in comparison to other substrates.

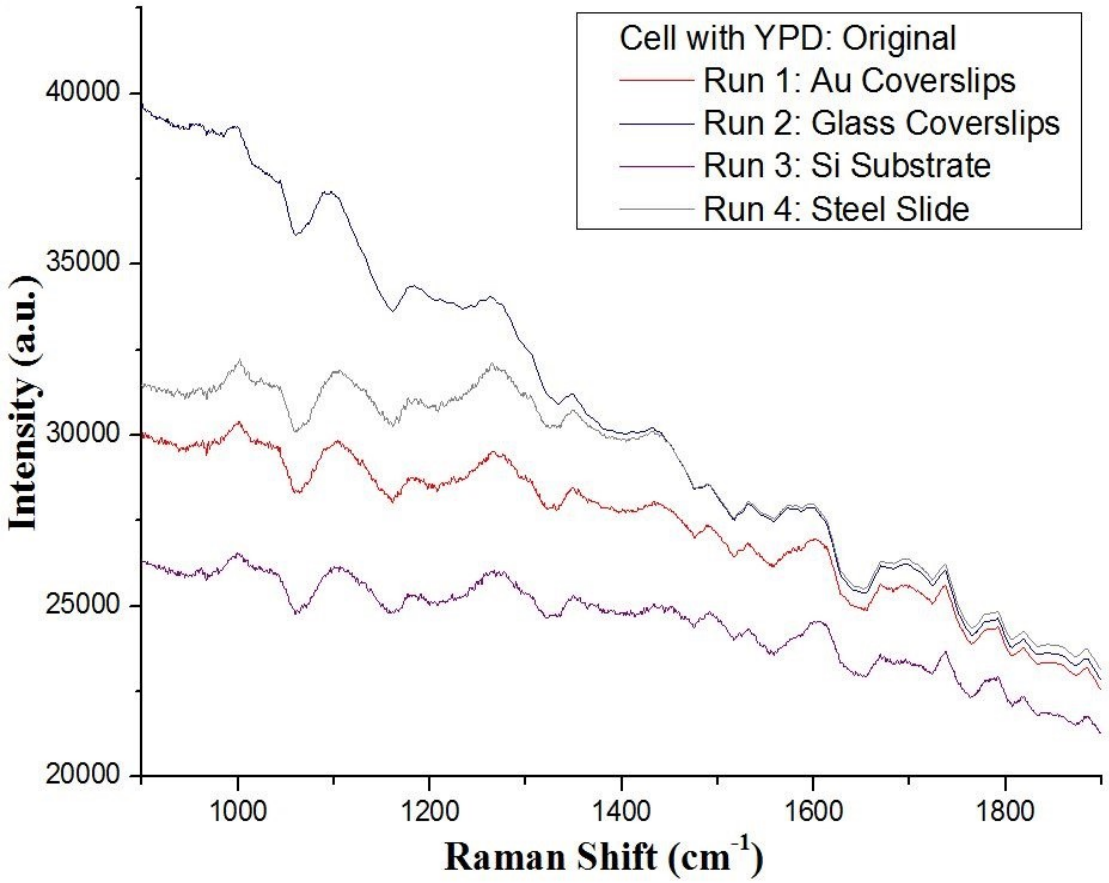

Fig. 4.21 Raman spectra of yeast cells with YPD medium (900-1900 cm^{-1})

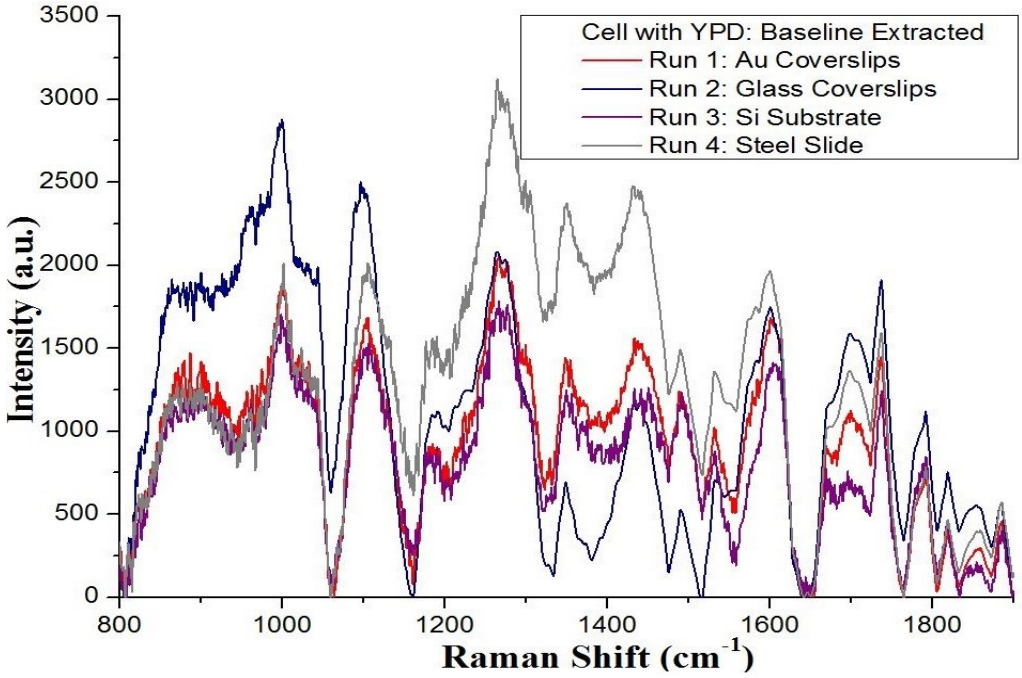

Fig. 4.22 Baseline extracted Raman spectra of yeast cells with YPD medium from Fig. 4.21

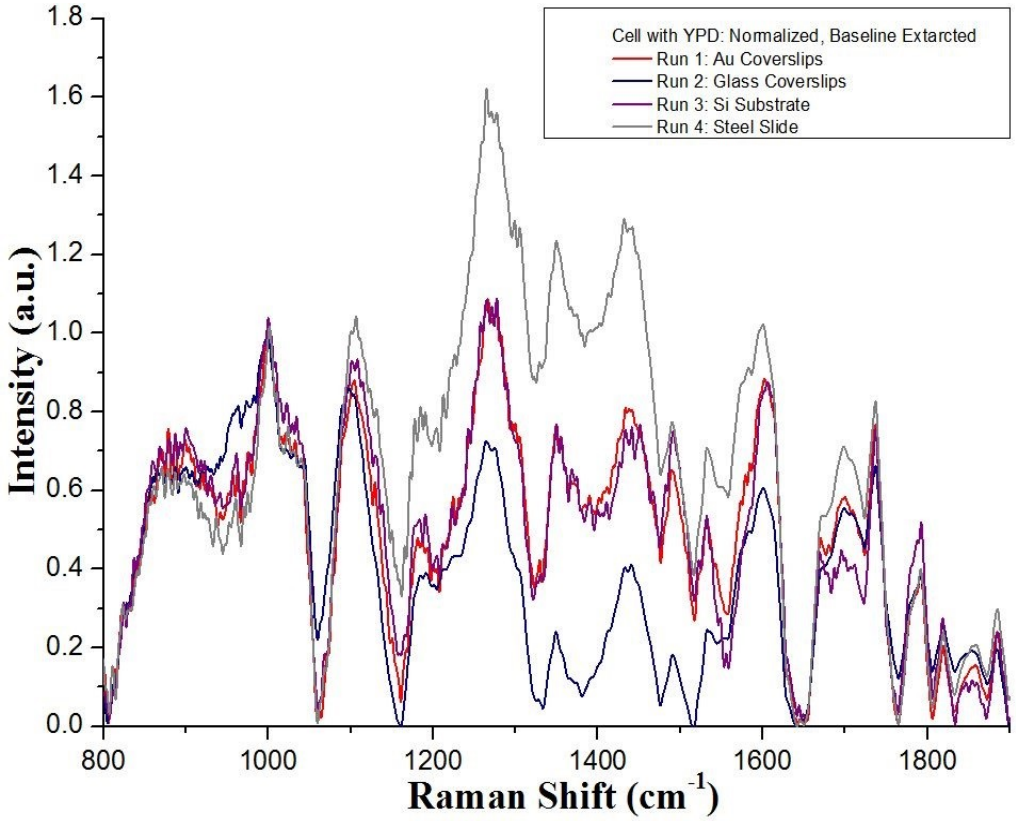

Fig. 4.23 Baseline extracted and normalized Raman spectra of yeast cells with YPD medium (800-1900 cm^{-1}) from Fig. 4.21

Fig. 4.24 presents normalized Raman spectra of yeast cells in YPD medium and YPD medium without live cells on Si wafers, to compare these two spectra. In Fig. 4.24 there are only minor differences observed between the cell culture and cell-free medium. Generally, a similarity of Raman spectra from yeast cells in YPD medium and YPD without live cells is not entirely surprising, since the YPD medium contains an extract of similar yeast cells. From Fig. 4.24, slight differences of relative intensities between the two spectra are observed at bands of 1265 cm^{-1} and 1276 cm^{-1}, 1438 cm^{-1}, 1490 cm^{-1}, 1603 cm^{-1}, 1670 cm^{-1} and 1700 cm^{-1}.

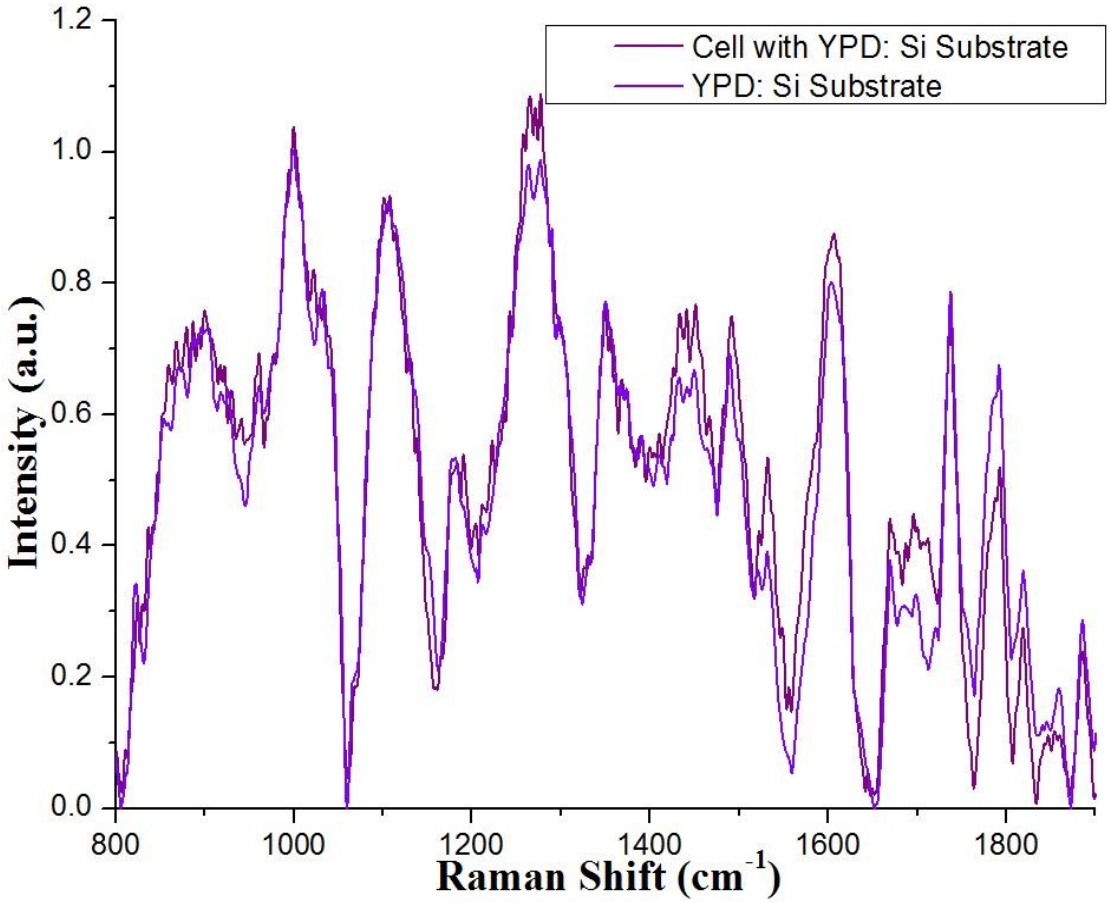

Fig. 4.24 Comparison of Raman spectra for yeast cells in YPD medium and cell-free YPD on Si wafers (800-1900 cm^{-1})

Fig. 4.25 compares normalized Raman spectra of yeast cells in YPD medium with a similar cells-containing sample, where fullerenol was added in the concentration of 20 μg/mL. In the figure, differences in Raman intensities mostly near 1350 cm^{-1} and 1590 cm^{-1} regions are discernible, which might be due to fullerenol's C-C stretches and ring stretches respectively (see Table 4.4).

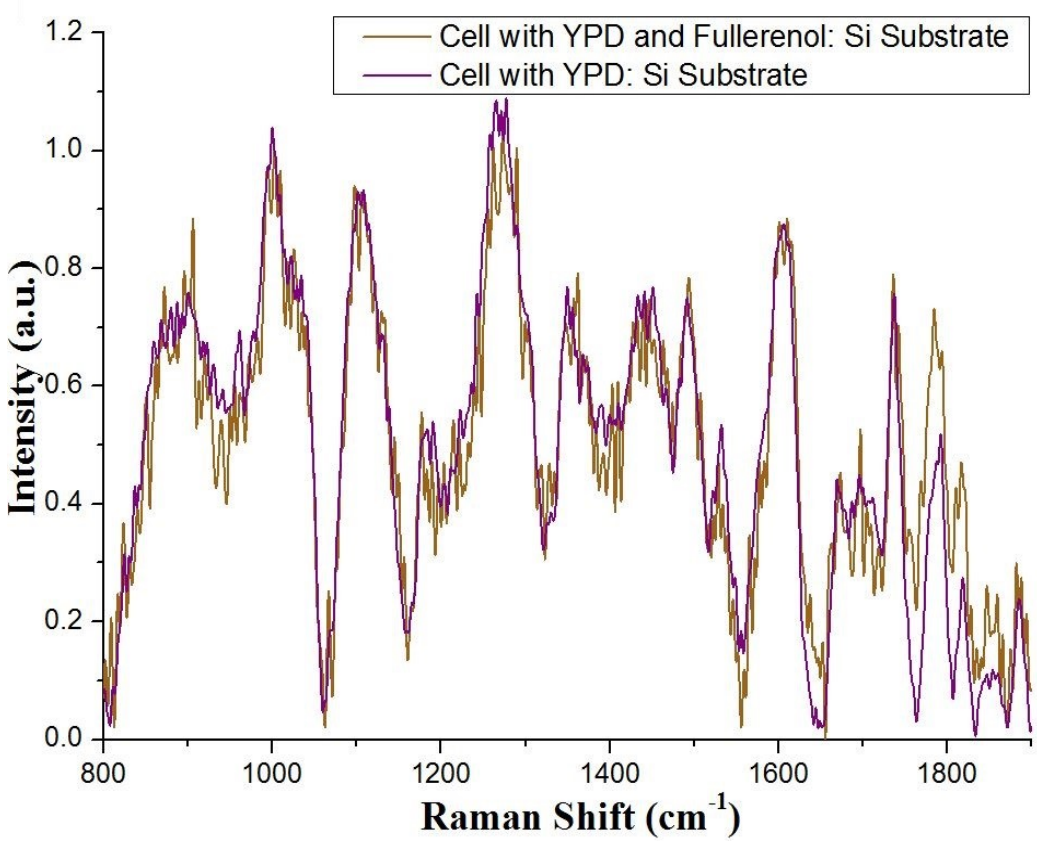

Fig. 4.25 Comparison of Raman spectra for yeast cells in YPD medium with fullerenol added, and cells in YPD medium on Si wafers (800-1900 cm^{-1})

Table 4.5 compiles published IR and Raman band assignments in various live cell cultures [101,102,103,104,105,106]. In the table, amide I and III bands correspond to Raman-active vibration modes of proteins' main chain [107]; whereas Trp, Phe and Tyr indicate residues tryptophan, phenylalanine, and tyrosine, each of which contains a Raman active aromatic

ring in their side chain. Other Raman-active components involve DNA and RNA, as well as lipids from cell membranes. Some of Raman bands observed in cell cultures are non-specifically attributed to C–C, C–H, C–O, C=C, and C=O vibrations.

Table 4.5 IR and Raman Band Assignments in Live Cells

Band Assignments [101-106]	**Published Raman Shifts, cm^{-1}**
Phe, Tyr, DNA, RNA	615-645 [102]
DNA/RNA	720-728 [106,104]
Trp Ring	750-760 [106]
Protein Residues, DNA/RNA Backbone Stretching, CH_2 Rocking	780-788 [106,104,102]
C –C, C-O-C, Trp, Tyr,	800-900 [106,102]
C-H, Metabolic Products, C-C Backbone	930-970, 1700 [106,103,102]
C –C, Protein Residues, Phe ring	999-1006 [106,103,104,102]
C –C Phe Ring Bend	1023-1034 [106,102]
C-C Lipids, C-N, C-O, DNA/RNA backbone	1050-1108 [106,105,103,104,102]
C –C, C-O, Lipids, Glucose, C-N	1124-1131 [106,102,101]
C-C, COH	1156 [106]
Protein Residues, C-O, C-H, Tyr	1171-1182 [106,102]
Carotenoids	1191-1193, 1213-1215 [106]
Proteins (Amide III), Tyr, Phe	1200-1300 [106,103,102]
DNA/RNA	1235, 1248-1257 [103,104,101]
Lipids, CH_2 Deformation	1265-1298 [105,103,102]
DNA/RNA, Protein Residues, Trp Ring, CH_2, CH_3	1332-1349 [106,103,104,102]
DNA/RNA, Protein Residues	1351-1377 [106,104,102,101]
CH_3	1395 [106]
DNA/RNA, Protein Residues, Lipids, Mitochondria, CH_2 Deformation, CH, CH_2, CH_3 Bending	1422-1451 [103,104,102,101]
CH_3	1461 [102]
DNA/RNA	1489, 1492 [104,102]
Carotenoids	1511-1535 [106]
Trp	1549-1554 [106,102]
Mitochondria, DNA/RNA, Aromatic Rings, C=C Phe	1575-1603 [104,102,101]
Trp, Phe, Tyr	1605-1618 [106]
Proteins (Amide I), Lipids C-O, C=C	1645-1670 [106,105,103,104,102]
Lipids C=O	1721,1737 [102]

Fig. 4.26 presents baseline extracted, smoothened, and normalized Raman spectra of yeast cells in YPD medium in the shift range from 800 cm^{-1} to 1800 cm^{-1}. The tentative band assignments shown on the figure have been done based on the information in Table 4.5. The Raman spectra in the figure show bands corresponding to C-C stretches at 900 cm^{-1}, 999 cm^{-1} and between 1023 cm^{-1} and 1034 cm^{-1}; bands from vibrations in lipids between 1100 cm^{-1} and 1108 cm^{-1}; C-H/metabolic products bands at 960 cm^{-1} and 1700 cm^{-1}; a C-O/ band at 1182 cm^{-1}; lipids/CH_2 deformation bands between 1265 cm^{-1} and 1276 cm^{-1}; DNA/RNA bands at 1349 cm^{-1}, 1492 cm^{-1} and 1603 cm^{-1}; a lipids band at 1438 cm^{-1}; a trp/carotenoid band at 1532 cm^{-1}; an amide I/ lipids band at 1670 cm^{-1} and finally, a C=O/ lipids band at 1737 cm^{-1}.

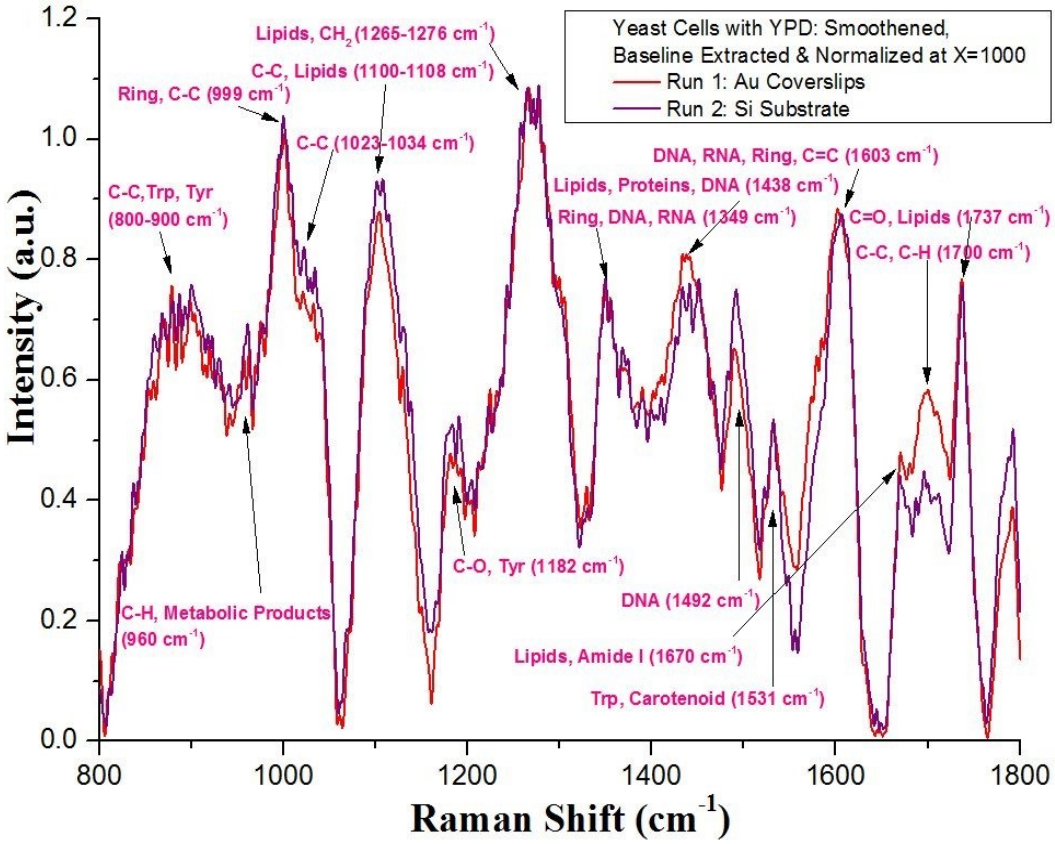

Fig. 4.26 Raman spectra of yeast cells in YPD medium on Au-coated glass coverslip and Si wafer with band assignments (800-1800 cm^{-1})

4.3.2 Analysis of HeLa Cell Cultures. Basic methods used to culture HeLa cells are described in Sect. 3.3.1. After trypsinization, a 1:2 dilution of cells was prepared in a 15 mL tube by adding 500 µL of cells stock (see Sect. 3,3,1) and 1 mL of fresh medium, and then pipetting the mixture up and down to mix it properly. Then, substrates comprising 13 mm glass cover slips coated with a 20 nm layer of Au and similar coverslips without Au were placed in a 6-well plate. The next step was to add 300 µL of the cells mixture from the 15 mL tube into each compartment. This was achieved by pipetting the mixture on the coverslips very carefully, and keeping the well plate immobile for 20 minutes so that the cells are let attaching on the substrates. Finally, 600 µL of fresh medium was added slowly at side of the well plate to make the final cells dilution equal to 1:2. Subsequently, the well plate was incubated at 37 °C in a humidified atmosphere for about 48 hours.

Raman measurements were performed after approximately 48 hours of incubating of the HeLa cells. The cells were cultured on either Au coated coverslips of ordinary glass coverslips as described above. Before the Raman measurements, the substrates with HeLa cells grown on them were first taken out from the well plate and transferred to a glass slide, which was washed with a 70% ethanol and dried. Afterwards, 60 µL of the medium solution from a specific compartment of the well plate was pipetted onto substrates to maintain the cell viability during the Raman measurements.

Raman spectra of the samples were collected with a Horiba LabRAM HR 800 instrument (Sect. 3.1.3) using a 532 nm excitation wavelength. The confocal hole size was kept at 200 µm, the objective had a 10X magnification, and 10 accumulation cycles of 10 s each were used for all the samples. The Lab Spec 5 software was used to collect

Raman spectra, and the Origin software was used to process and analyze the results. Before collecting Raman spectra, optical microscopic images of the cells were collected. An example image of HeLa cells on a glass substrate is shown in Fig 4.27.

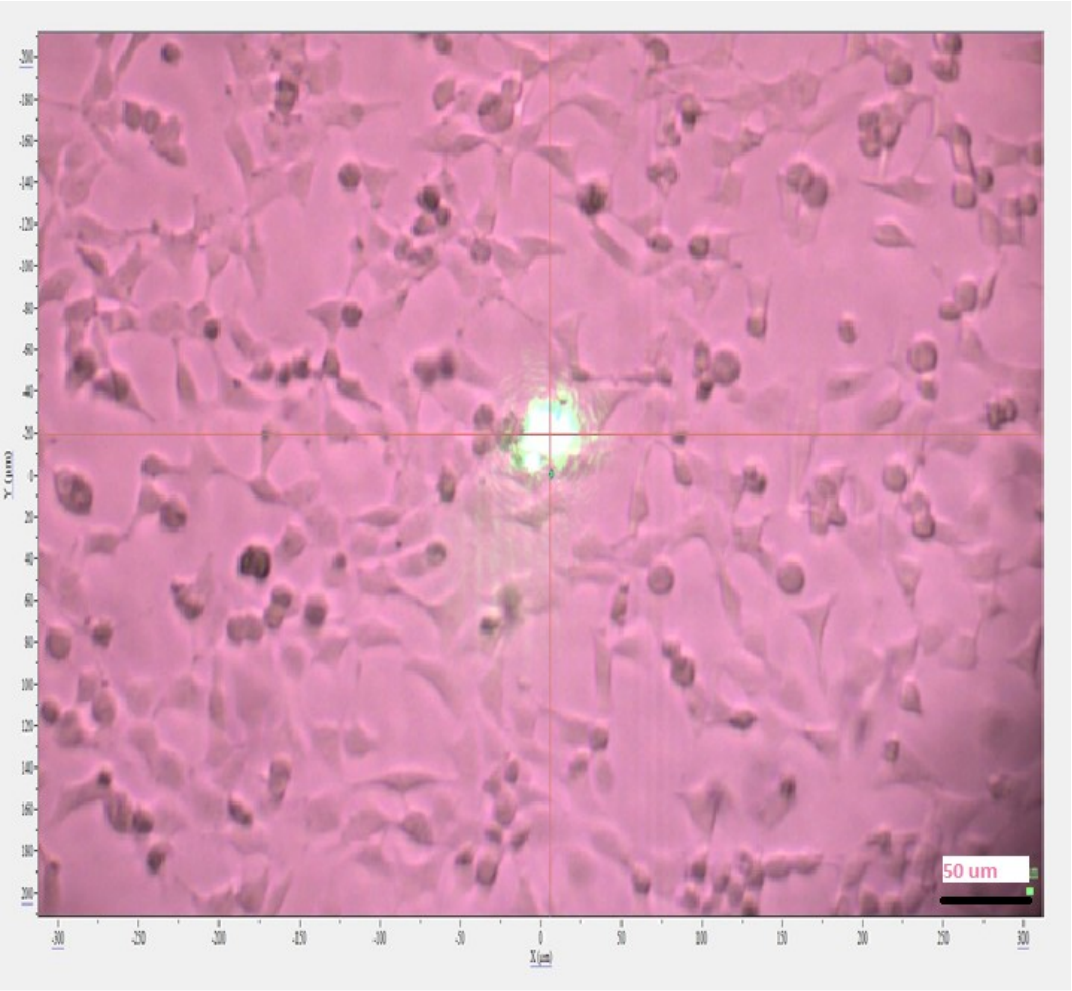

Fig. 4.27 Optical microscopic image of HeLa cells on a glass substrate

Fig. 4.28 shows two raw Raman spectra on glass substrates, where one spectrum represents HeLa cells on a glass substrate with L-15 medium, and another one is a spectrum of the medium alone on a similar glass substrate without cells. After collecting of the raw spectra, baseline extraction using a fourth-degree polynomial and normalization at 1101 cm^{-1} were done.

The corresponding baseline-extracted and normalized spectra are shown in Fig. 4.29. The figure also shows tentative band assignments done based on the literature data listed in Table 4.5 from Sect. 4.3.1. The assignments shown in the figure include C-C stretches between 800 cm^{-1} and 917 cm^{-1}, at 994 cm^{-1}, and between 1023 cm^{-1} and 1039 cm^{-1}; lipid bands between 1100 cm^{-1} and 1108 cm^{-1}; C-O/protein residue bands at 1176 cm^{-1} and 1195 cm^{-1}; lipids/CH_2 deformation bands between 1268 cm^{-1} and 1277 cm^{-1}; DNA/RNA bands at 1349 cm^{-1}, 1492 cm^{-1} and 1603 cm^{-1}; lipids bands at 1433 cm^{-1}; a trp/carotenoids band at 1531 cm^{-1}; an amide I/ lipids band at 1670 cm^{-1}; and a C=O/ lipids band at 1737 cm^{-1}.

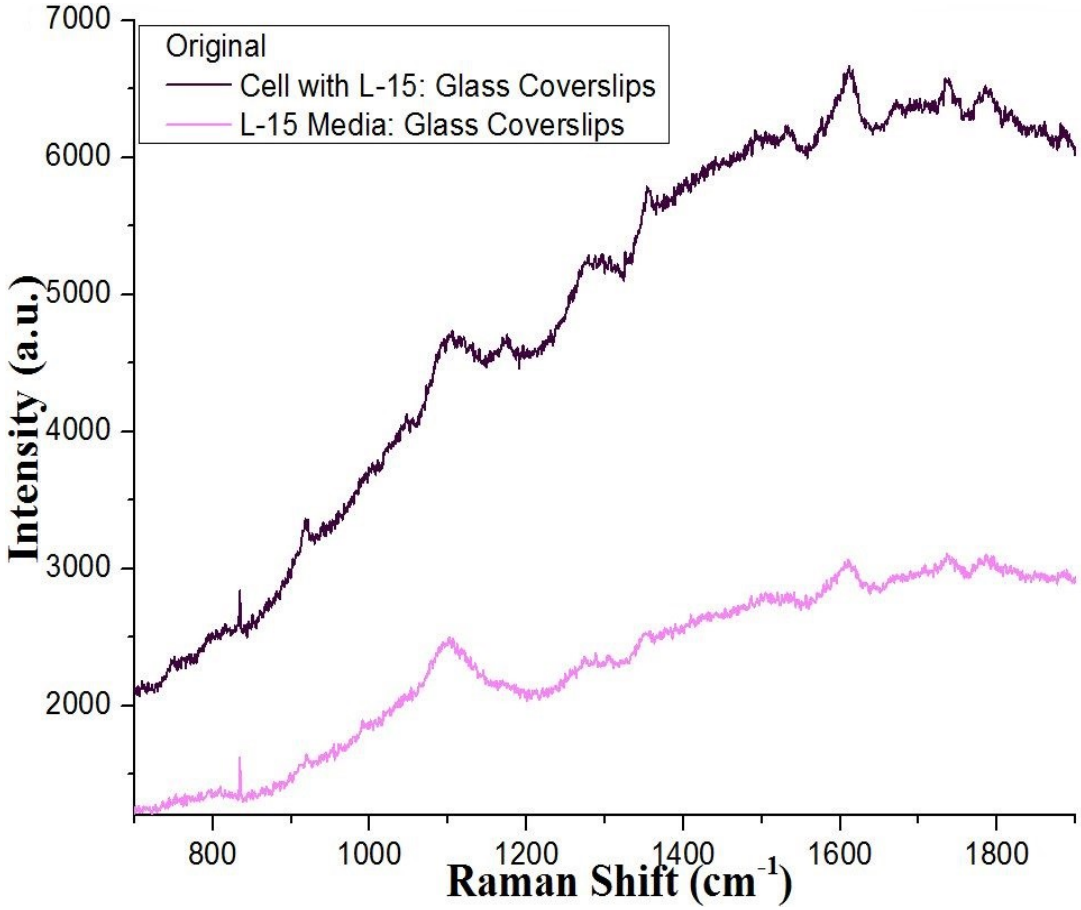

Fig. 4.28 Raman spectra of HeLa cells with L-15 medium and L-15 medium alone (700-1900 cm^{-1})

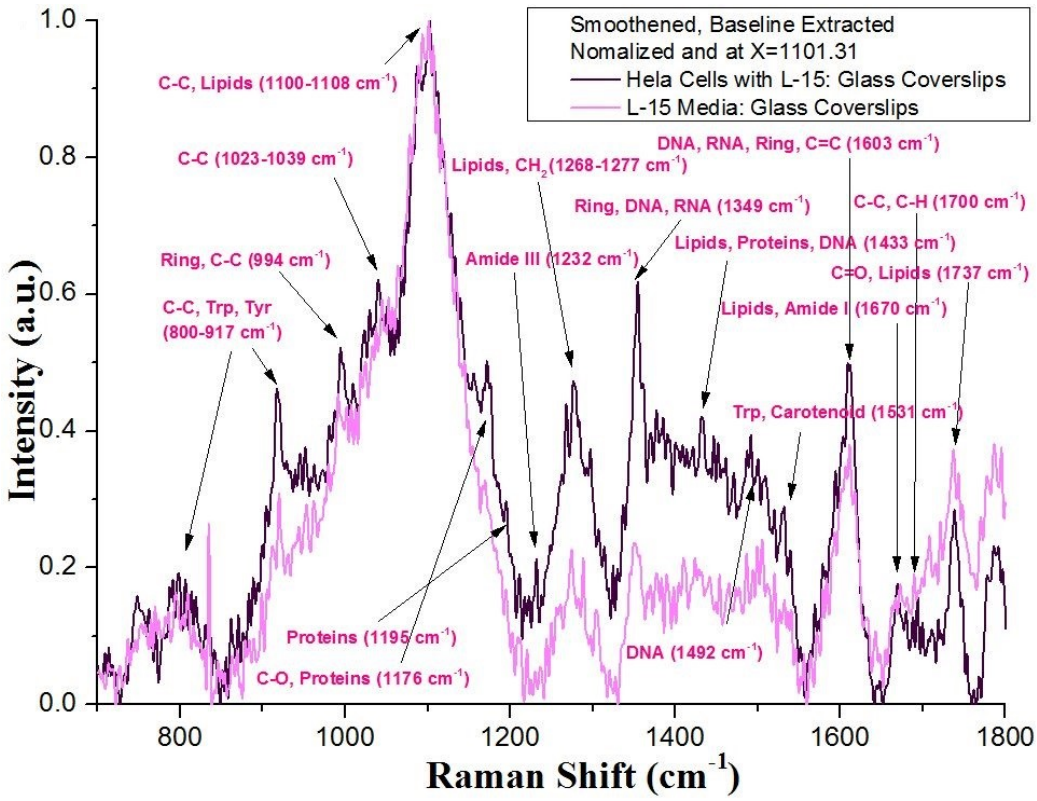

Fig. 4.29 Baseline-extracted and normalized Raman spectra of HeLa cells with L-15 medium and L-15 medium alone on glass coverslips with band assignments (700-1800 cm^{-1})

4.3.3 SERS of HeLa Cells. In order to investigate possible influence of surface enhancement of the Raman scattering on the HeLa cells characterization, glass substrates with a deposited Au layer were used in some of the experiments, as described in Sect. 4.1.2. Fig. 4.30 compares the Raman spectra of HeLa cells with and without a 20 nm thick Au layer on the glass slide. The spectra were baseline extracted using a fourth degree polynomial, smoothened, and normalized at 1101 cm^{-1}, similarly to the procedures used to compare the other spectra in this work. From the figure, it is evident that the Raman shifts are almost the same for both spectra. However, when the Au coated slide was used as a substrate, intensities of most major Raman bands were significantly higher in comparison to the ordinary glass slide without the Au coating. The reason of the

enhancement is that deposited Au layers possess a surface roughness that results in a buildup of electromagnetic hot-spots that enhance the Raman scattering, as explained in Sects. 2.3 and 2.4.

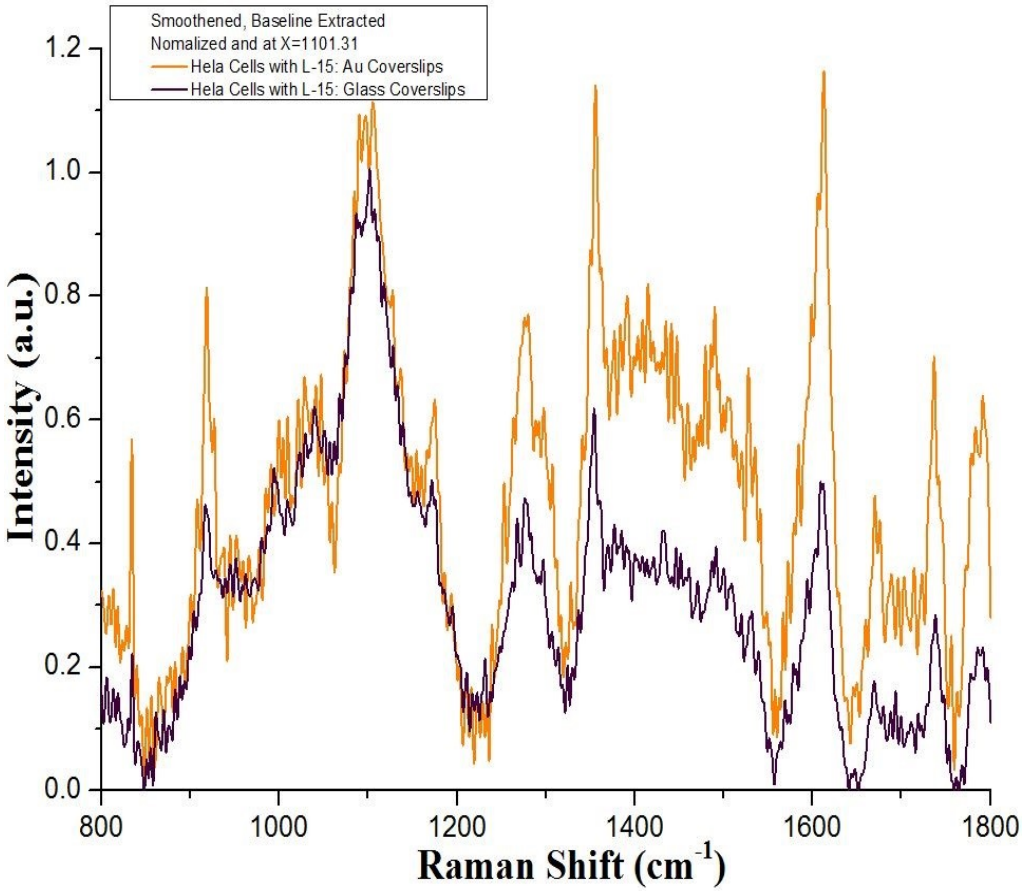

Fig. 4.30 Comparison of Raman spectra of HeLa cells with and without a 20 nm Au layer on the substrate (800-1800 cm^{-1})

In particular, pronounced enhancement was observed for the Raman bands at 917 cm^{-1}, between 1100-1108 cm^{-1}, at 1176 cm^{-1}, between 1268-1277 cm^{-1}, at 1349 cm^{-1}, at 1492 cm^{-1}, at 1531 cm^{-1}, at 1603 cm^{-1}, at 1670 cm^{-1}, at 1737 cm^{-1} and at 1792cm^{-1} corresponding to C-C stretches, the lipids band, C-O/proteins residue bands, CH_2 deformation bands, DNA/RNA bands, trp/carotenoids bands, amide I bands and finally, C=O vibrations.

5. DISCUSSION

5.1 Results Achieved from this Research

In this work, a primary objective was to optimize and develop protocols for acquiring Raman spectra of liquid samples, mainly biological samples in solution and on a substrate, using the LabRAM instrument. The challenge was to collect pronounced Raman spectra while minimizing the power and acquisition time, so that sample damage could be avoided. Resolving this involved shorter scanning ranges in order to minimize the time and to get a higher Raman signal. Another challenge of working with biological samples is a high fluorescence background, which was dealt with by turning on the intensity correction option to avoid the fluorescence effect. The optimized protocols for biological samples were further improved by maximizing intensities of the signal from the samples, eliminating the background noise, and selecting a proper objective lens, filters, and exposure time. Initially, the experiments were done using a 785 nm laser and by keeping the intensity correction option off, which didn't work well, as it produced very low signal to noise ratio. Afterwards, another approach was followed, using the same laser wavelength and keeping the intensity correction on, which was able to produce a Raman signal from the samples. However, the bands still were not pronounced enough due to the noise. Next, I used a 532 nm laser and kept the intensity correction option off, which allowed to reduce the fluorescence. However, the signal quality was still unsatisfactory. The next step was to keep the intensity correction on, which reduced the background to a significant extent and improved the signal intensity as well. These setting were used to collect all Raman spectra described in this work. To optimize the

laser power intensity based on the heat tolerance capabilities of my liquid samples, several steps were taken. First, the objective lens with a larger spot size and longer working distance should be selected, for which reason a 10X objective lens was chosen. The lens was kept at a safe distance from the samples. Different filters also were attempted, however, this strategy worsened the signal to noise ratio. Finally, to minimize the scanning and acquisition time of the sample, both the acquisition and scanning times were varied from 25 seconds to 25 minutes, and the optimal time was selected based on the signal quality. The specific optimal times varied depending on the samples and of the quantity of the liquid during the Raman measurements.

As the obtained Raman spectra for biological samples were complex with many bands due to the involvement of a broad variety of biological materials in live cells, to gain a better understanding of the Raman scattering phenomenon, I have done both experiments and modeling studies for simpler carbon-based systems. In order to model Raman bands, 8 models of functionalized graphene were constructed using the VESTA software. The constructed models were optimized and their Raman bands calculated using DFT with the Quantum ESPRESSO code [66-68]. From comparative analysis of the results from the DFT calculations and published DFT data, it was concluded that most predicted C–C bending and stretch bands fall into 330-1100 cm^{-1} and 832-1074 cm^{-1} regions in the structures considered; predicted C–H vibration bands are found in a narrower region between 1273 cm^{-1} and 1375 cm^{-1}, however, some C–C stretch modes are also found in these regimes; ring vibration modes are observed between 704 and 796 cm^{-1}, and also at 1325-1616 cm^{-1}; and O–H vibration bands are localized at 3716 cm^{-1}.

In order to interpret and compare the experimental results of similar carbon materials with the calculated Raman bands, Raman spectra were collected for several graphene derivatives: oxidized nano graphene platelets mixed with deionized (DI) water; a graphene oxide (GO); and fullerenol ($C_{60}(OH)_n$) solution. It was found that these graphene compounds exhibit pronounced bands around 760-794 cm^{-1}, 841 cm^{-1}, 1090 cm^{-1}, 1345 cm^{-1}, 1362 cm^{-1}, 1592 $cm^{-1,}$ and beyond 3000 cm^{-1}. Based on the DFT predictions, the first two sets of bands can be attributed to ring vibration and C–C skeletal stretch, respectively, whereas the band at 1090 cm^{-1} is due to C–C bending. The bands observed at 1345 cm^{-1} and 1362 cm^{-1} have been attributed to C–C vibrations, and that at 1592 cm^{-1} is due to ring stretch. The bands of 3240 cm^{-1} and 3422 cm^{-1} observed in the graphene platelets sample arise from O-H bond vibrations.

After successfully interpreting the Raman bands of simpler carbon-based systems, I have proceeded to studies of two examples of biological samples. These included live yeast cells samples, and live HeLa cells samples, which were characterized. The two cell cultures are substantially different morphologically, as yeast cells are grown in solution, whereas HeLa cells are cultured on the surface of substrates.

I have compared my results for yeast cells with published data. Fig. 5.1 represents a recently published [101] Raman spectrum of a single yeast cell on a Si substrate coated with Ag microparticles, in the shift range from 700 cm^{-1} to 1900 cm^{-1}. Many bands seen in Fig 4.26 of this work are also found at close positions in Fig. 5.1, although the amplitudes of individual maxima differ. In particular, the Raman spectrum in Fig. 4.26 shows a band corresponding to phe stretches at 999 cm^{-1}, whereas in Fig. 5.1 a similar band can be seen at approximately 1000 cm^{-1}; I observe lipids/CH_2 deformation or

protein vibration bands between 1265 cm^{-1} 1276 cm^{-1} and at 1438 cm^{-1}, whereas in Fig. 5.1 such bands are found at 1300 $cm^{-1}$and at 1446 cm^{-1}; in Fig. 4.26 DNA/RNA bands occur at 1349 cm^{-1}, 1492 cm^{-1} and 1603 cm^{-1}, and in Fig. 5.1 DNA bands are assigned to spectral maxima at 1360 cm^{-1} and 1584 cm^{-1}; and finally, bands corresponding to vibrations of double bonds such as C=O are seen close to 1670 cm^{-1} in both figures. One can conclude that the positions of most bands found in yeast cells in this work are reasonably compatible with the published data. The differences in relative heights of individual peaks could be attributed to different morphologies of the sample, as well as a difference in background extraction procedures.

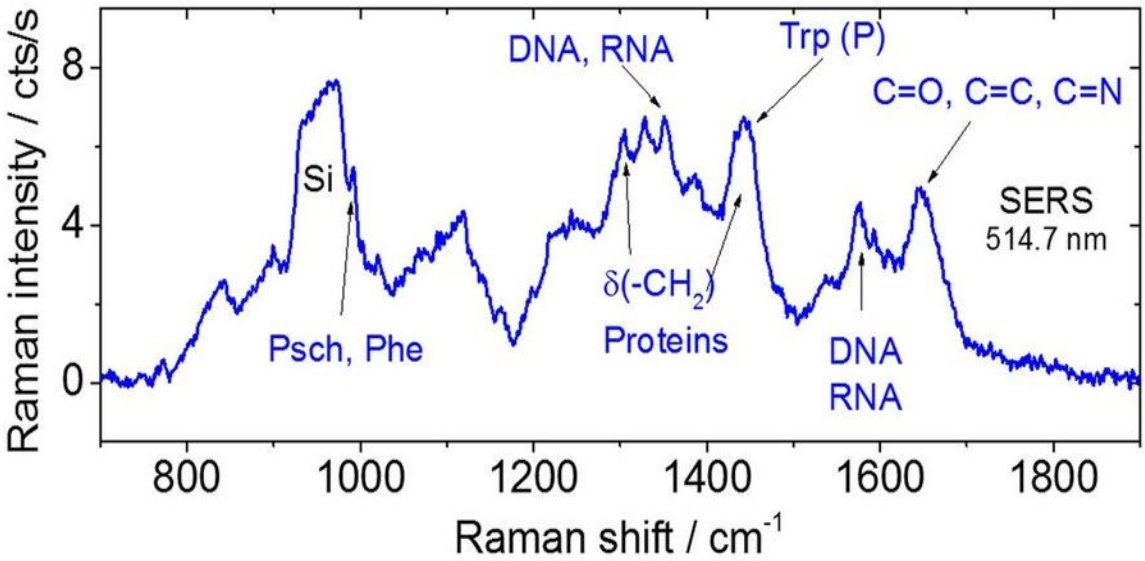

Fig. 5.1 Raman spectrum of a single yeast cell on a Si substrate coated with Ag microparticles using a 514.7 nm laser. Reproduced from [101] with permission.

Next, I have compared Raman bands observed in my work for the yeast and HeLa cells. Fig. 5.2 compares the spectra of the two cultures. Despite these cell cultures are very distant evolutionarily, from Fig. 5.2 it is evident that the spectra of yeast and HeLa cells show Raman shifts at very close locations.

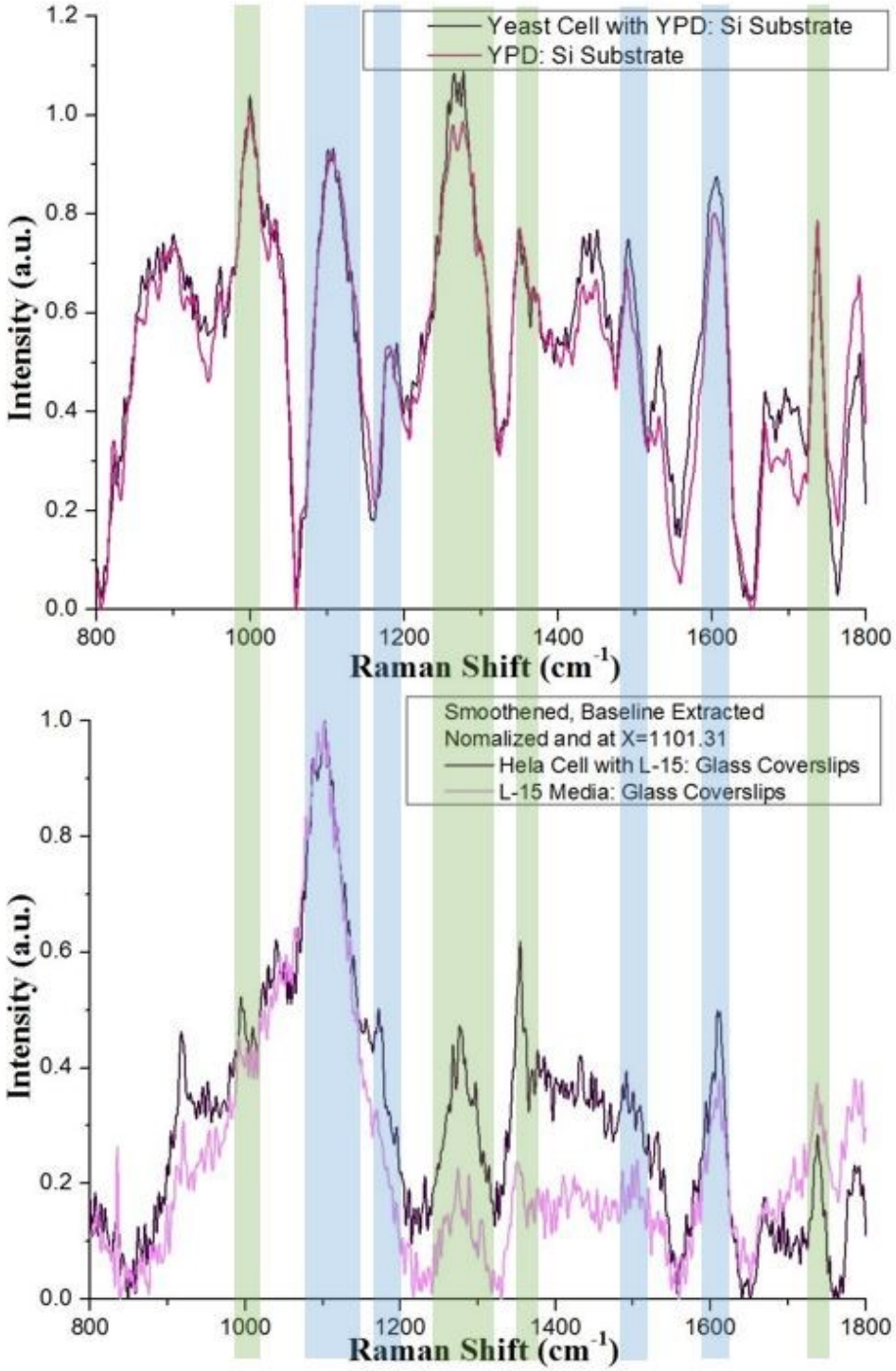

Fig. 5.2 Comparison of Raman spectra for yeast cells (top) and HeLa cells (bottom), and their respective media. The vertical translucent bars highlight bands for which similar shifts were observed in the two cultures. Blue bars mark bands that exhibit similar relative intensities, whereas green bars mark bands that are pronouncedly different in relative intensities.

To further illustrate this similarity, Table 5.1 lists the respective positions of major bands in yeast and HeLa cells, and Table 5.2 (first column) lists the bands that are found at similar locations. On the other hand, differences in relative intensities have been detected in several bands for yeast and HeLa cell cultures, particularly representing vibrations from proteins, DNA/RNA, and cell membranes. The relative intensity for bands of yeast cell culture is stronger than that of HeLa cell culture near 990 cm^{-1} and between 1267-1277 cm^{-1}; whereas at 1737 cm^{-1}, HeLa cells have a stronger Raman signal compared to yeast cells. These differences are summarized in the right column of Table 5.2. Since SERS enhancement was not a factor in neither of the spectra in Fig. 5.2, the different intensities may be attributed to evolutionary and morphological differences of the cell cultures.

Table 5.1 Raman bands positions and assignments in yeast and HeLa cells

Band Types [101-106]	Raman Shifts (cm^{-1}) Yeast Cells	Raman Shifts (cm^{-1}) HeLa Cells
C –C, C-O-C, Trp, Tyr	800-900	800-917
C-H, Metabolic Products	960	---
C –C, Aromatic Ring of Phe	999	994
C –C Phe	1023-1034	1023-1039
C –C, Lipids	1100-1108	1100-1108
C-O, C-H, Tyr	1182	1176, 1195
Lipids, CH_2 Deformation	1265-1276	1268-1277
Proteins, Aromatic Ring, DNA, RNA	1349	1349
CH_2, Lipids, Proteins, DNA, RNA	1438	1433
DNA, RNA	1492	1492
Trp, Carotenoids	1531	1531
DNA, RNA, Aromatic Rings, C=C	1603	1603
Proteins (Amide I), Lipids, C-O, C=C	1670	1670
C-C, C-H	1700	---
C=O, Lipids	1737	1737

Table 5.2 Comparison of Raman bands intensities in yeast and HeLa cells

Similar Raman Shifts (cm^{-1})	Different Relative Intensities (cm^{-1})
999/994	Strong 999 / Weak 994
1100/1100	-
1181/1176	-
1265-1276/1268-1277	Strong 1265-1276 / Medium 1268-1277
1349/1349	Medium 1349 / Strong 1349
1492/1492	-
1603/1603	-
1737/1737	Strong 1737 / Medium 1737

In addition to the Raman spectra of two cell cultures, Fig. 5.2 also depicts spectra of the corresponding media. For yeast cells in solution, only a minor difference was observed between the cell medium and living cells. In contrast, for HeLa cells on a glass substrate, a significant difference was observed between intensities of bands representing vibrations in proteins (1349 cm^{-1}), DNA/RNA (1433 and 1603 cm^{-1}), and lipids (1268 and 1737 cm^{-1}) against the L15 medium. Note that both yeast and HeLa cells exhibit differences against the corresponding media at similar Raman shifts, only the differences for yeast cells are less pronounced, hypothetically because of a relatively lesser number of yeast cells captured in the light focus in solution.

Upon demonstrating a proof-of-principle Raman characterization of the two cell cultures, attempts to achieve an enhancement of the Raman scattering have been made. For this purpose, a 20 nm Au coting was created on glass substrates used for the Raman measurements of both cell cultures. Surface roughness of the Au coating was expected to produce electromagnetic hot-spots required for the enhancement. For yeast cells, I could not detect the enhancement, hypothetically because most yeast cells were contained in the liquid at a distance from the Au-coated surface of the substrate. However, for HeLa cells, most of the bands were enhanced due to the rough SERS substrate, as Fig. 4.30

illustrates. From these observations, I can conclude that nanostructured Au coatings on glass substrates offer a strong potential for the enhancement of Raman bands from substrate-confined biological samples.

5.2 Problems Encountered During Experiments

During this work, many challenges were dealt with while learning how to work with the cell cultures and collect Raman spectra for liquid biological samples.

- The first challenge was to learn the techniques of growing HeLa cell cultures, as a Physics student. This was successfully resolved.

- An even bigger challenge faced in this work was to collect high-quality Raman spectra of liquid samples despite a strong fluorescent background that the samples produced. After an extensive optimization work, a satisfactory Raman signal from the samples was obtained.

- A related, yet different challenge was to find the correct laser excitation wavelength, based on the power intensity. The power at the spot size needed to be minimized in order to avoid thermal damage of the biological samples, while maintaining a satisfactory quality of the spectrum. A solution of this is described in Sect. 4.1.1.

- The next challenge was to optimize the scanning range and accumulation time to get as strong as possible Raman intensity from many molecular species contained in the cells. Optimal selection of these was found dependent of the sample, as discussed in Sect. 5.1.

- The final challenge was to collect Raman spectra for yeast cells in solution. These cells were not grown on the substrate and instead, they were capable moving during the Raman measurements. Also most of the cells were at a distance from the substrates, challenging SERS measurements with Au coatings deposited on the substrates. Although encouraging results have been obtained as described in Sect. 4.3, achieving a full strength enhancement of Raman spectra from live yeast cells may require different approaches beyond the scope of this thesis.

6. CONCLUSIONS AND FUTURE WORK

6.1 Conclusions

In this thesis, experimental protocols for Raman characterization of liquid samples, mainly biological samples, were developed and optimized for the LabRAM 800 micro-Raman instrument. This was achieved by minimizing the acquisition time, performing shorter scanning, and turning on the intensity correction option to avoid the fluorescence effect.

In order to facilitate interpretation of Raman bands in complex multicomponent samples, I have also investigated a simpler benchmark example of graphene based materials, both experimentally and computationally. Raman spectra were collected from: oxidized graphene platelets mixed with water; fullerenol solution; and dried solution of graphene oxide. The spectra exhibit pronounced Raman bands. In order to elucidate the trends in various graphene compounds, and validate the band assignments, in-vacuum density-functional theory (DFT) calculations of molecular vibrations in several graphene-based models were also performed using the Quantum ESPRESSO software. In the computational study, models were built for pristine graphene and graphene functionalized with hydrogen, oxygen, and hydroxyl groups of various C/H, C/O and C/OH ratios, respectively. The calculations predict a rich pattern of Raman bands originating from vibrations of various bonds and atomic groups. Based on these predictions and comparisons with the literature, band assignments for the experimental spectra of graphene based materials have been made.

Raman spectra of two cell cultures, yeast and HeLa, were acquired and interpreted. In addition to evolutionary differences, the two types of cells represent distinctly different morphologies, since yeast cells are cultured in solution, whereas HeLa cells grow on a substrate.

The Raman characterization of yeast cells in solution revealed pronounced Raman bands: including those corresponding to proteins, DNA/RNA, and lipids. Positions of major bands are very similar to the recently published Raman spectrum of yeast cells fixed on a substrate [101]. However, the spectra for yeast cell media show only minor differences against those of living cells, for the reason of the presence of dried yeast extract in the cell media.

For HeLa cells, major Raman bands were observed at positions close to those of yeast cells; however, relative intensities of bands representing vibrations in proteins, lipids, and DNA/RNA were different against the L15 medium. Importantly, a pronounced enhancement of several Raman bands of the HeLa cells spectra was observed using a glass substrate with a deposited Au layer, promising a strong potential of SERS as a method of characterization of HeLa cells cultures.

6.2 Proposed Future Works and Considerations

- In future experiments with cell cultures, it may be advantageous to measure the Raman spectra of cells contained in a simpler buffer solution such as a phosphate buffered saline (PBS), rather than in cell culture media. Comparing the results with the Raman spectra of the buffer solutions would produce greater differences, facilitating the analysis of molecular vibrations in the cells.

- It may be interesting to collect Raman spectra after fixing yeast cells on a substrate. This will allow the yeast cells to remain on the substrate, rather than moving in solution during Raman measurements.

- There is a strong potential of the enhancement of Raman spectra from cells grown on, or fixed at, SERS substrates bearing plasmonic nanostructures. Continuing such experiments with different plasmonic nanostructure designs may lead to interesting future works. In regard of the substrate selection for cells cultures characterization, quartz or CaF_2 might be considered because of their low background signals.

REFERENCES

1 P. Alivisatos, “The Use of Nanocrystals in Biological Detection”, *Nature*, 2004; 22: 47-52

2 K. K. Alharbi, and A. A. Yazeed, “Role and Implications of Nanodiagnostics in the Changing Trends of Clinical Diagnosis”, *Saudi Journal of Biological Sciences*, 2014; 21(2): 109–117

3 M. Longmire, P. L. Choyke, et. Al., “Clearance Properties of Nano-sized Particles and Molecules as Imaging Agents: Considerations and Caveats”, *Nanomedicine (London, England)*, 2008; 3(5): 703–717

4 D. Pal, C. K. Sahu, et. al., “*Bhasma*: The Ancient Indian Nanomedicine”, *Journal of Advanced Pharmaceutical Technology & Research,* 2014; 5(1): 4–12

5 P. D. Howes, R, Chandrawati, et. al., “Colloidal Nanoparticles as Advanced Biological Sensors”, *Science,* 2014; 346 (6205): 1247390-10

6 S. Mitragotri, D. G. Anderson, et al., “Accelerating the Translation of Nanomaterials in Biomedicine”, *American Chemical Society,* 2015; 9: 6644-654

7 J. X. Cheng and X. S. Xie, “Vibrational Spectroscopic Imaging of Living Systems: An Emerging Platform for Biology and Medicine”, *Science*, 2015; 350(6264): 8870-8879

8 A. F. Chrimes, K. Khoshmanesh, et al., “Microfluidics and Raman Microscopy: Current Applications and Future Challenges”, *Chem. Soc. Rev.,* 2013; 42: 5880-5096

9 A. Campion and P. Kambhampati, “Surface-Enhanced Raman Scattering”*, Chem. Soc. Rev.,* 1998; 27: 241-250

10 J. A. Dieringer, et al., “Surface Enhanced Raman Spectroscopy: New Materials, Concepts, Characterization Tools, and Applications”, *Faraday Discuss,* 2006; 132: 9-26

11 C. L. Haynes, et al., “Surface-Enhanced Raman Spectroscopy”, *Anal. Chem.,* 2005; 77: 338A-346A

12 P. L. Stiles, et al., “Surface-Enhanced Raman Spectroscopy”, *Annu. Rev. Anal. Chem.,* 2008; 1: 601-626

13 E. Petryayeva, U. J. Krull, “Localized Surface Plasmon Resonance: Nanostructures, Bioassays and Biosensing- A Review”, *Elsevier*, 2011; 706: 8-24

14 P. G. Etchego, and E. C. Le Ru, “A perspective on Single Molecule SERS: Current Status and Future Challenges”, *Phys Chem Chem Phys.,* 2008; 10; 6079-6089

15 M. Doshi, S. Mitragotri, “Designer Biomaterials for Nanomedicine”, *Adv. Funct. Mater.,* 2009; 19: 3843–3854

16 M. A. Dobrovolskaia, S. McNeil, “Immunological Properties of Engineered Nanomaterials”, *Nat. Nanotechnol.,* 2007; 2: 469–478

17 M. L. Etheridge, S. A. Campbell, A. G. Erdman, et al., “The Big Picture on Nanomedicine: The State of Investigational and Approved Nanomedicine Products”, *Nanomedicine,* 2013; 9:1 –14

18 B. Bohunicky, and S. A. Mousa, “Biosensors: The New wave in Cancer Diagnosis”, *Nanotechnology, Science and Applications*, 2011; 4: 1–10

19 “Benefits and Applications”, National Nanotechnology Initiative Available: http://www.nano.gov/you/nanotechnology-benefits

20 X. Yang, M. Yang, B. Pang, et al., “Gold Nanomaterials at Work in Biomedicine*”, Chem. Rev.,* 2015; 115: 10410-10488

21 R. Popovtzer, A. Agrawal, N. A. Kotov, et al., “Targeted Gold Nanoparticles Enable Molecular CT Imaging of Cancer”, *Nano Lett.,* 2008; 8: 4593−4596

22 G. Zhu, L. Mei, et. al., “Nanomedicine”, *The Scientist,* 2014; 40598

23 B. Schrader, *“*Infrared and Raman Spectroscopy*”*, *VCH Publishers Inc.: New York*, 1995; Chapter 4

24 C. V. Raman and K. S. Krishnan, “A New Type of Secondary Radiation”, *Nature*, 1928; 121: 501–502

25 C.H. Camp, M.T. Cicerone, “Chemically Sensitive Bioimaging with Coherent Raman Scattering”, *Nat. Photonics,* 2015; *9:* 295–305

26 J.W. Chan, “Recent Advances in Laser Tweezers Raman spectroscopy (LTRS) for Label-Free Analysis of Single Cells”, *J. Biophoton.,* 2013; *6:* 36–48

27 I. H. Boyaci,H. T. Temiz,H. E. Geniş, E. A. Soykut, N. N. Yazgan, B. Güven, R. S. Uysal,A. G. Bozkurt, K. Ilaslan, O. Torun and F. C. D. Şeker, “Dispersive and FT-Raman Spectroscopic Methods in Food Analysis”, *Royal Society of Chemistry,* 2015; 5: 56606-56624

28 M. Fleischmann, P. J. Hendra, A. J. McQuillan, “Raman Spectra of Pyridine Adsorbed at a Silver Electrode”, *Chem Phys Lett,* 1974; 26: 163-166

29 D. L. Jeanmaire, and R. P. Van Duyne, "Surface Raman Spectroelectrochemistry: Part I. Heterocyclic, Aromatic, and Aliphatic Amines Adsorbed on the Anodized Silver Electrode", *J Electroanalytical Chemistry and Interfacial Electrochemistry*, 1977; 84: 1-10

30 W. E. Doering, and S. M. Nie, "Single-Molecule and Single-Nanoparticle SERS: Examining the Roles of Surface Active Sites and Chemical Enhancement", *J. Phys. Chem. B,* 2002; 106: 311-317

31 P. G. Etchego, and E. C. Le Ru, "A perspective on Single Molecule SERS: Current Status and Future Challenges", *Phys Chem Chem Phys.,* 2008; 10; 6079-6089

32 M. Moskovits, "Surface-Enhanced Raman Spectroscopy: a Brief Retrospective", *J. Raman Spectroscopy,* 2005; 36: 485-496

33 T. Iliescu, M. Baia, D. Maniu, "Raman and Surface-Enhanced Raman Spectroscopy on Molecules of Pharmaceutical and Biological Interest", *Romanian Reports in physics*, 2008; 60: 829-855

34 J. P. Camden, *et al.*, "Probing the Structure of Single-Molecule Surface-Enhanced Raman Scattering Hot Spots", *J. Am. Chem. Soc.,* 2008; 130: 12616

35 L. Jensen, *et al.*, "Electronic Structure Methods for Studying Surface-Enhanced Raman Scattering", *Chem. Soc. Rev.,* 2008; 37: 1061-1073

36 E. Petryayeva, U. J. Krull, "Localized Surface Plasmon Resonance: Nanostructures, Bioassays and Biosensing- A Review", *Elsevier*, 2011; 706: 8-24

37 K. A. Willets, R. P. V. Duyne, "Localized Surface Plasmon Resonance Spectroscopy and Sensing", *Annu. Rev. Phys. Chem.,* 2007; 58: 267–97

38 M. Rycenga, P. H. C. Camargo, et al., "Understanding the SERS Effects of Single Silver Nanoparticles and Their Dimers, One at a Time", *The journal of physical chemistry letters*, 2010;1: 696-703

39 W. Cai, et al., "Investigation of Surface-Enhanced Raman Scattering from Platinum Electrodes using a Confocal Raman Microscope: Dependence of Surface Roughening Pretreatment", *Surface Science,* 1998; 406: 9–22

40 K. Kneipp, Y. Wang, et al., "Single Molecule Detection Using Surface-Enhanced Raman Scattering (SERS)", *Phys. Rev. Lett.,* 1997; 87: 1667-1670

41 R. F. Peters, L. Gutierrez-Rivera, S. K. Dew, M. Stepanova, "Surface Enhanced Raman Spectroscopy Detection of Biomolecules Using EBL Fabricated Nanostructured Substrates", *J. Vis. Exp.,* 2015; 97

42 R. E. C. Le, *et al.*, "Surface Enhanced Raman Scattering Enhancement Factors: A Comprehensive Study", *J. Phys. Chem. C,* 2007; 111: 13794-13803

43 B. Sharma, R. R. Frontiera, et al., "SERS: Materials, Applications, and The Future", *Materialstoday,* 2012; 15: 16-25

44 W. A. Paxton, S. L. Kleinman, et. al., "Surface-Enhanced Raman Spectroelectrochemistry of TTF-Modified Self-Assembled Monolayers", *J. Phys. Chem.,* 2011; 2: 1145-1149

45 K. Kneipp, Y. Wang, et. al., "Single Molecule Detection Using Surface-Enhanced Raman Scattering (SERS)", *Physical Review Letters*, 1997; 78: 1667-1670

46 Y. S. Huh, A. J. Chung, et. al., "Surface Enhanced Raman Spectroscopy and Its Application to Molecular and Cellular Analysis, *Microfluid Nanofluid*, 2009; 6:285–297

47 J. A. Dieringer, K. L. Wustholz, et. al., "Surface-Enhanced Raman Excitation Spectroscopy of a Single Rhodamine 6G Molecule", *J. Am. Chem. Soc.,* 2009; 121 (2): 849-854

48 C. Netti and H. Stanford, "Applications of Reproducible SERS Substrates for Trace Level Detection", *Raman Technology for Today's Spectroscopists,* 2006; 8-17

49 R. Smith, K. L. Wright, et. al., "Raman spectroscopy: An Evolving Technique for Live Cell Studies", *Royal Society of Chemistry*, 2016; 141: 3590–3600

50 A. Ralph, A. R. Tripp, and et. al., "Novel nanostructures for SERS Biosensing", *NanoToday*, 2008; 3: 31-37

51 S. Lecomte, H. Wackerbart, and et. al., "Time-Resolved Surface-Enhanced Resonance Raman Spectroscopy for Studying Electron-Transfer Dynamics of Heme Proteins", J. *Am. Chem. Soc.*, 1998; 120: 7381-7382

52 T. V. Dinh, L. R. Allain, D.L. Stokes, "Cancer Gene Detection using Surface-Enhanced Raman Scattering (SERS)", *Journal of Raman Spectoscopy*, 2002; 33: 511–516

53 Y. S. Li, J. S. Church, "Raman Spectroscopy in the Analysis of Food and Pharmaceutical Nanomaterials", *Journal of Food and Drug Analysis,* 2014; 22; 29-48

54 D. Yang and Y. Ying, "Applications of Raman Spectroscopy in Agricultural Products and Food Analysis: A Review", *Applied Spectroscopy Reviews,* 20122; 45: 539-560

55 S. Kenneth, Sladin, S. E. Miller, "Light Microscopy", Biology Reference Forum Available: http://www.biologyreference.com/La-Ma/Light-Microscopy.html

56 Bradbury, Savile, and B. Bracegirdle, “Introduction to Light Microscopy”,*New York: Springer-Verlag*, 1998 –book

57 “Light Microscopy”, Experimental Bioscience,
Available: http://www.ruf.rice.edu/~bioslabs/methods/microscopy/microscopy.html

58 “AE30/31 Inverted Microscope”, Motic,
Avilable: http://www.ionoptix.com/wp-content/uploads/2014/07/AE31.pdf

59 Y. L. Wang and D. L. Taylor, “Fluorescence Microscopy of Living Cells in Culture Part A. Fluorescent Analogs, Labeling Cells, and Basic Microscopy”, *Academic Press*, 1989; 2: 207-237 –Book

60 “CCD Detector”, Horiba Scientific,
Available: http://www.horiba.com/us/en/scientific/products/raman-spectroscopy/raman-academy/raman-faqs/what-is-a-ccd-detector/

61 “LabRAM Series”, Horiba Scientific,
Available:
https://www.horiba.com/fileadmin/uploads/Scientific/Documents/Raman/labrambro.pdf

62 “LabRAM HR”, Horiba Scientific,
Available:
http://www.horiba.com/fileadmin/uploads/Scientific/Documents/Raman/LabRAM_HR_Evolution.pdf

63 “What Types of Laser (Rayleigh) Filtering are Used?”, Horiba Scientific,
Available: http://www.horiba.com/us/en/scientific/products/raman-spectroscopy/raman-academy/raman-faqs/what-types-of-laser-rayleigh-filtering-are-used/

64 “532 BPF”, IRIDIAN SPECTRAL TECHNOLOGIES,
Available: http://www.iridian-optical-filters.com/product/532-bpf/

65 “Laboratory Fume Hoods”, ESCO,
Available: http://www.escoglobal.com/fume-hoods.php

66 “Quantum Espresso”, QUANTUMESPRESSO,
Available: http://www.quantum-espresso.org

67 G. Kresse and J. Hafner, “Ab. Initio Molecular Dynamics for Liquid Metals”, *Phys. Rev. B: Condens. Matter Mater. Phys., 1993;* 47: 558-561

68 G. Kresse and J. Hafner, “Efficiency of Ab-Initio Total Energy Calculations for Metals and Semiconductors Using a Plane-Wave Basis Set” *Comp. Mat. Sci.,* 1996; 6: 15-50

69 G. Kresse and J. Furthmüller, “Efficient Iterative Schemes for Ab Initio Total-Energy Calculations Using a Plane-Wave Basis Set", *Phys. Rev. B*, 1996; 54: 11169

70 T. H. Fsischer and J. Almlof, “General Methods for Geometry and Wave Function Optimization”, *J Phys Chem,* 1992; 96: 9768–9774

71 K. Momma and F. Izumi, “VESTA: A Three-Dimensional Visualization System for Electronic and Structural Analysis”, *J. Appl. Crystallogr.,* 2008; 41: 653-658

72 K. Momma and F. Izumi, “Commission on Crystallographic Computing”, *IUCr Newsletter,* 2006; 7: 106

73 F. Izumi and K. Momma, “Three-Dimensional Visualization in Powder Diffraction”, *Solid State Phenom.,* 2007; 130: 15-20

74 “VESTA”, *JP-Minerals*, 2016;
Available: http://jp-minerals.org/vesta/en/

75 A. F. Palonpon, J. Ando, et.al., “Raman and SERS Microscopy for Molecular Imaging of Live Cells”, *Nature Protocols*, 2013; 8:677-692

76 C. B Schaffer, A. Brodeur, et. al., “Laser-Induced Breakdown and Damage in Bulk Transparent Materials Induced by Tightly Focused Femtosecond Laser Pulses”, *Measurement Science and Technology*, 20001; 12: 1784-1794

77 Y. Fu , H. Wang, et, al., “Characterization of Photodamage in Coherent Anti-Stokes Raman Scattering Microscopy”, *Optics Express*, 2006; 14: 3942-3951

78 D. M. P. Hoffmann, K. Kuhnke, et, al., “Sum-Frequency Generation Microscope for Opaque and Reflecting Samples”, *Review of Scientific Instruments*, 2002; 73:3221

79 F. Liu, P. Ming, and J. Li, “Ab Initio Calculation of Ideal Strength and Phonon Instability of Graphene Under Tension”, *Phys Rev B,* 2007; 76: 064120.1–064120.7

80 I. W. Frank, D. M. Tanenbaum, A. M. Zande, P. L. McEuen, “Mechanical Properties of Suspended Graphene Sheets”, *J Vac Sci Tech B,* 2007; 25: 2558–2561

81K. S. Novoselov, A. K. Geim, S. V. Morozov, D. Jiang, Y. Zhang,S. V. Dubonos, I. V. Grigorieva, A. A. Firsov, “Electric Field Effect in Atomically Thin Carbon Films”, *Science,* 2004; 306: 666-669

82 R. R. Nair, P. Blake, A. N, Grigorenko, K. S. Novoselov, T. J. Booth, T. Stauber, N. M. R. Peres, A. K. Geim, “Fine Structure Constant Defines Visual Transparency of Graphene”, *Science,* 2008; 320: 1308–1308

83 F. Wang, Y. B. Zhang, C. S. Tian, C. Girit, A. Zettl, M. Crommie, Y. R. Shen, "Gate-Variable Optical Transitions in Graphene", *Science,* 2008; 320:206-209

84 S. Ghosh, I. Calizo, D. Teweldebrhan, E. P. Pokatilov, D. L. Nika, A. A. Balandin, W. Bao, F. Miao, and C. N. Lau, "Extremely High Thermal Conductivity of Graphene: Prospects for Thermal Management Applications in Nanoelectronic Circuits", *Appl Phys Lett,* 2008; 92: 151911.1–151911.3

85 A. A. Balandin, S. Ghosh, W. Z. Bao, I. Calizo, D. Teweldebrhan, F. Miao, C. N. Lau, "Superior Thermal Conductivity of Single-Layer Graphene", *Nano Lett,* 2008; 8:902-907

86 A. K. Geim and K. S. Novoselov, "The Rise of Graphene", *Nature Materials*, 2007; 6: 183 – 191

87 B. Liu, H. Sun, T. Peng, G. Ji, "Molecular Vibrational Spectroscopy Characterization of Epoxy Graphene Oxide from Density Functional Calculations", *J Mol Model*, 2013; 19: 1429–1434

88 V. V. Ivanovskaya, A. Zobelli, D. Teillet-Billy, N. Rougeau, V. Sidis, and P.R. Briddon, "Hydrogen Adsorption on Graphene: A First Principles Study", *Eur. Phys. J. B,* 2010; 76: 481–486

89 M. Rocha, A. D. Santo, et al., "Ab-initio and DFT Calculations on Molecular Structure, NBO, HOMO–LUMO Study and a New Vibrational Analysis of 4-(Dimethylamino) Benzaldehyde", *Spectrochimica Acta Part A: Molecular and Biomolecular Spectroscopy*, 2015; 136: 635-643

90 D. M. Gil, M. E. Tuttolomondo, et al., "DFT Calculations of Structure and Vibrational Properties of 2,2,2-Trichloroethylacetate, CH3CO2CH2CCl3", *Spectrochimica Acta Part A: Molecular and Biomolecular Spectroscopy*, 2014; 123:290-297

91 H. Gökce and S. Bahçeli, "Molecular Structure, Spectroscopic Properties and DFT Calculations of 2_(Methylthio)nicotinic Acid", *Optics and Spectroscopy,* 2013; 115: 469-483

92 V. Arjunan, L. Devi, et al., "A New Look into Conformational, Vibrational and Electronic Structure Analysis of 3,4-Dimethoxybenzonitrile", *Spectrochimica Acta Part A: Molecular and Biomolecular Spectroscopy,* 2013; 113: 302-313

93 R. Sekine, E. G. Robertson, et al., "Raman, Infrared and Computational Analysis of Genistein and its Methoxy Derivatives", *Vibrational Spectroscopy*, 2011; 57: 306– 314

94 L. Szabo, K. Herman, et al., "Surface-Enhanced Raman Scattering and DFT Investigation of Eriochrome Black T Metal CHeLating Compound", *Spectrochimica Acta Part A: Molecular and Biomolecular Spectroscopy,* 2011; 79: 226-231

95 A. Bebu, L. Szabo, et al., “IR, Raman, SERS and DFT Study of Amoxicillin”, *Journal of Molecular Structure*, 2011; 993; 52-56

96 V. Mukherjeea, N.P. Singh, et al., “FTIR and Raman spectra, DFT and Normal Coordinate Computations of 2,4,5- and 2,4,6-Tri-Fluoroanilines”, *Spectrochimica Acta Part A: Molecular and Biomolecular Spectroscopy,* 2009; 73:249-256

97 K. Sowoidnich and H. D. Kronfeldt, “Fluorescence Rejection by Shifted Excitation Raman Difference Spectroscopy atMultipleWavelengths for the Investigation of Biological Samples”, *ISRN Spectroscopy*, 2012

98 A. Barth, “Infrared Spectroscopy of Proteins”, *Biochimica et Biophysica Acta* , 2007; 1767: 1073–1101

99 D. L. Vien, N.B. Colthup, et al., “The Handbook of Infrared and Raman Characteristics Frequencies of Organic Molecules”, *Academic Press: Boston*, 1991

100 The optical density measurements is the courtesy of Jonathan Short from the Department of Biology of the MSU.

101 L. Mikoliunaite, R. D. Rodriguez, et, al., “The Substrate Matters in the Raman Spectroscopy Analysis of Cells”, *Scientific Reports*, 2015; 5:13150

102 S. Dochow, N. Bergner, et. al., “Classification of Raman Spectra of Single Cells with Autofluorescence Suppression by Wavelength Modulated Excitation”, *Anal. Methods,* 2013; 10: 1039

103 P. Candeloro, L. Tirinato, et. al., “Nanoparticle Microinjection and Raman Spectroscopy as Tools for Nanotoxicology Studies”, *Analyst*, 2011; 136: 4402-4408

104 H. H. Lin, A. Yu, et, al., “Single Nuclei Raman Spectroscopy for Drug Evaluation”, *Anal. Chem*., 2012; 84: 113-112

105 L. Hartsuiker, N. J. L. Zeijen, et. al., “A Comparison of Breast Cancer Tumor Cells with Varying Expression of the Her2/neu Receptor by Raman Microspectroscopic Imaging”, *Analyst*, 2010; 135: 3320-3326

106 K. Sowoidnich, H. D. Kronfeldt, “Fluorescence Rejection by Shifted Excitation Raman Difference Spectroscopy at Multiple Wavelengths for the Investigation of Biological Samples”, *ISRN Spectroscopy*, 2012; 2012: 11 pages